Nanoscale Advances

ROYAL SOCIETY OF CHEMISTRY

PAPER

Published on 13 July 2026
Licensed under CC-BY-NC 4.0

Check for updates

Cite this: DOI: 10.1039/d6na00187d

Combining high throughput and precision: millifluidic production of magnetic nanoparticles for biomedical applications

Lennart Göpfert,[ad] Max Schoenen,[ad] Eva Miriam Buhl,[b] Thomas Weirich,[c] Thomas Schmitz-Rode[d] and Ioana Slabu *[ad]

Magnetic nanoparticles (MNP) offer great potential for applications in nanomedicine and regenerative medicine. For successful clinical translation, scalable and standardized manufacturing methods are crucial to enable the production of MNP with tailored properties and high yields. Here, we present a modular and automated millifluidic synthesis system for MNP production. The system comprises five independently controllable interconnected units, allowing precise tuning of synthesis parameters in each unit and continuous production to reach high throughput. Comprehensive characterization was conducted using high-resolution transmission electron microscopy, dynamic light scattering, and magnetometry, while application-relevant performance was evaluated by magnetic hyperthermia, magnetic resonance imaging, and magnetic particle imaging. A production yield of up to 93%, enabling the synthesis of approximately 680 g_{Fe} MNP per day was achieved. By varying the reaction temperature, MNP sizes from 17 nm to 27 nm were obtained. Reproducibility experiments consistently demonstrated good agreement. In depth analysis confirms high crystalline structure, narrow size distributions, and excellent magnetic properties. MNP showed remarkable performance as heating agents in magnetic hyperthermia with an intrinsic loss power of 5.4 $nHm^2\ kg^{-1}$, outperforming commercially available MNP. They had good contrast agent capabilities in magnetic resonance imaging (r_2 = 529 1/mMs) and moderate ones in magnetic particle imaging. The reproducible, scalable and automated synthesis system provides a robust platform for producing functional MNP, supporting their application in biomedical imaging, targeted therapies, and future clinical translation.

Received 8th March 2026
Accepted 3rd July 2026

DOI: 10.1039/d6na00187d

rsc.li/nanoscale-advances

1 Introduction

Magnetic nanoparticles (MNP) are increasingly investigated for their use in magnetic fluid hyperthermia (MFH) and drug delivery, as they offer unique superparamagnetic properties and functionality.[1–4] Recently, MNP have been incorporated into scaffolds, enabling magnetically controlled release of growth factors in regenerative medicine or tumor ablation in cancer treatment.[5–8] Several MNP-based products, such as Feridex®, NanoTherm®, and Resotran®, are already on the market as contrast agent for magnetic resonance imaging (MRI) and heating agents for MFH, while MRI-visible hernia implants have entered clinical use.[9–11] As an emerging imaging modality, Magnetic Particle Imaging (MPI) enables background-free, real-time imaging of MNP by exploiting their nonlinear magnetization, promising high sensitivity and quantification.[12]

For new applications, overcoming hurdles to reach clinical translation requires among tailored application specific MNP-characteristics, many regulatory considerations, pre- and clinical studies to demonstrate robust patient safety, efficacy of the therapy and commercial considerations.[13–15] Consequently, this requires manufacturing processes that can be carried out reliably, robustly, reproducibly and on a large scale. In most cases, manual handling protocols to synthesize MNP have high technical variability, lack of precision or power and show low throughput production. In addition, manually performed syntheses require expertise and training. Using automated, continuous processes in MNP manufacturing can overcome these limitations, enabling highly scalable, reproducible, cost-effective, and environmentally friendly production of MNP with tailored properties.[16]

Scaling is an important requirement in the early stages of development that should not be undervalued. For example, the production of magnetic scaffolds can require several hundred

[a]Institute of Medical Engineering, Helmut Schmidt University Hamburg, Holstenhofweg 85, 22043 Hamburg, Germany. E-mail: slabui@hsu-hh.de
[b]Institute of Pathology, Electron Microscopy Facility, RWTH University Hospital Aachen, Pauwelsstraße 30, 52074 Aachen, Germany
[c]Central Facility for Electron Microscopy, RWTH Aachen University, Ahornstr. 55, 52074 Aachen, Germany
[d]Institute of Applied Medical Engineering, RWTH Aachen University, Medical Faculty, Pauwelsstr. 30, 52074 Aachen, Germany

© 2026 The Author(s). Published by the Royal Society of Chemistry

grams of dry MNP per batch. Another hurdle is the design of MNP as high-performance hyperthermia and contrast agents.

To meet the growing demand of MNP for diagnostic and therapeutic applications, various synthesis methods have been developed. Biological approaches use magnetotactic bacteria, offering high biocompatibility and high heating performance but low yield.[17] Physical methods, such as ball milling or laser ablation, end in broad MNP size distributions.[18] Chemical methods, including thermal decomposition and precipitation, enable the production with high yields and tunable MNP properties.[19,20] Precipitation synthesis is preferred for scalability reasons, as it is operable with aqueous solutions at lower temperatures.[21–23] This method involves mixing an alkaline solution with an iron salt under stirring, introduced by Massart and Khalafalla.[24,25] Recently, continuous manufacturing in millifluidic and microfluidic flow regimes has been developed, offering superior MNP properties compared to batch synthesis.[26–32] These systems typically use a reactor to mix reactants, a tube coil for residence time adjustment, and pumps for liquid transport. Advanced mixing techniques, such as jet reactors, improve efficiency by creating strong turbulence, reducing mixing time.[23] Reaction quenching with additional reactants can be facilitated to prevent clustering.[33]

This paper presents a modular, continuous synthesis process for MNP production *via* oxidative precipitation. The process is designed for high yield and application-specific MNP properties. The quality of the resulting MNP was evaluated using transmission electron microscopy (TEM) to assess particle size and circularity, electron diffractometry to determine the crystalline structure, and dynamic light scattering (DLS) to measure the hydrodynamic diameter. Magnetization and cytotoxicity measurements were performed. Furthermore, their capability to be used as contrast enhancement, tracer and heating agents was investigated.

2 Experimental

In the following, a production process is introduced to enable high-scale continuous MNP production while tailoring properties for MFH, MRI and magnetic particle imaging (MPI). The system consists of five serially connected units (Fig. 1A–E). The first unit (Fig. 1A) consists of two peristaltic pumps (Boxer Pump 15 KS, Boxer GmbH, Germany) with stepper motors as drive (model DM556T, Stepperonline Inc., USA), which feed iron salts and bases into the system. The tubing is made of medical-grade thermoplastic elastomer (Innovaprene®, Suzhou Innovapure Co., Ltd, China). A custom-designed Arduino® feedback control system uses load-cell signals from the reactant reservoirs to continuously adjust the peristaltic pumps *via* a fast integral control loop, enabling stable and adjustable flow rates with a dosing accuracy of $\pm$ 0.1 mL s^{-1}. Each reactant has a dedicated pumping system, which simplifies process adjustments.

The second unit (Fig. 1B) mixes the reactants using a jet reactor with a T-piece (IQS-Standard, Sang-A Pneumatic Co., Korea) and an injection needle (Sterican®, B. Braun SE, Germany). Jet reactors provide superior mixing efficiency and scalability compared to simple T-pieces or micromixers due to their strong turbulence generation.[23] For a base and iron salt flow rate of 2.6 mL s^{-1} each, the flow rate ratio is $R_r = 18.75$, and the Reynolds number $Re_r = 1664$. This results in a mixing time

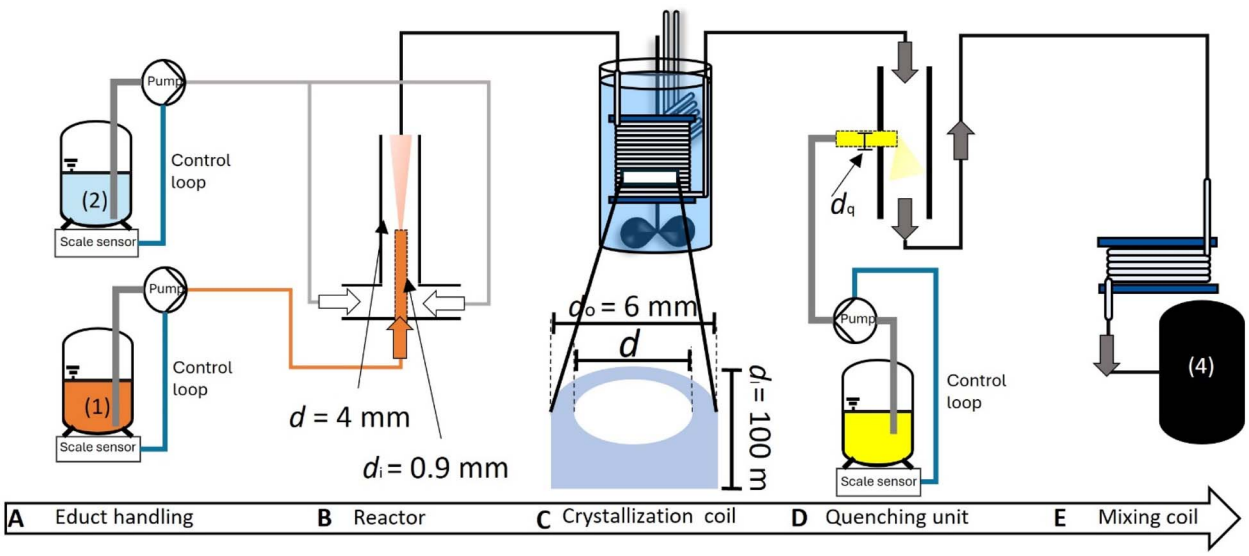


Fig. 1 (A–E) Outline of the millifluidic process for the continuous synthesis of MNP and respective properties. The process consists of the following units: (A) Educt handling with peristaltic pumps, reactant containers (1) for the iron salt and reactant container (2) for the base and corresponding control loop *via* weight sensors. (B) Reactor with a jet mixer. Geometries and sizes of the jet mixer and tubes used are displayed; jet mixer with an inner diameter of the jet inlet of $d_i = 0.9$ mm and tube diameter $d = 4$ mm (C) crystallization coil with a coiled tube in a water bath. Jet reactor with an inner diameter of the jet inlet of $d_i = 0.9$ mm and tube diameter $d = 4$ mm (D) quenching unit with citric acid injection with an inner diameter $d_i = 0.9$ mm quenching the synthesis of MNP in tube with $d_q = 3.5$ mm (Jet-Quench). (E) Mixing coil with a tube and product container. Table S2 in the SI summarizes the parameters characterizing the reactor and quench unit.

© 2026 The Author(s). Published by the Royal Society of Chemistry

of τ_{mix} << 10 ms (calculated according to [23] see Table S2 in the SI). In contrast, a batch reactor can require several seconds to achieve homogeneous mixing.[34] Shorter mixing times reduce local pH, and reactant concentration variations, which is crucial for controlling MNP properties.

The third unit (Fig. 1C) consists of a 100 m long PTFE crystallization coil (PTFE Tube Shop BV, Netherlands), where the reaction temperature can be adjusted from 20 to 98 °C in a 10 L water bath. PTFE is beneficial as it prevents MNP adherence due to its strong negative surface charge (<−40 mV) at pH > 10, reducing clogging effects.[35] A 2000 W immersion heater (Carl Roth GmbH + Co. KG, Germany) equipped with a two-point controller between the heating coil and a temperature sensor maintained a stable temperature (±1 °C). This unit significantly influences reaction conditions, as reaction temperature (T_r) directly impacts MNP properties. The coil has a total volume of 1.26 L, a flow rate of 5.2 mL s^{-1}, and a retention time of 4 min. The system ensures efficient heat transfer, enabling uniform crystal growth.[34]

The fourth unit (Fig. 1D) quenches the reaction by injecting citric acid (CA) through another jet mixer (Jet-Quench). CA stabilizes MNP in aqueous solutions and prevents aggregation of MNP.[36,37] Using an additional pump system (see above), CA is fed in at a flow rate of 2.6 mL s^{-1}, while the synthesis product flows at 5.2 mL s^{-1}, resulting in a flow rate ratio of $R_q = 12.09$ and $Re_q = 2496$. The mixing time remains below 10 ms.[23] CA quenching is used for producing MNP with core sizes < 10 nm.[33]

The fifth unit (Fig. 1E) transfers the MNP-CA solution through a 10 m tube into the product container. The millifluidic system, with an inner tube diameter of 4 mm, offers major advantages over microfluidic systems (<1 mm)[38] as the system enables a high throughput of 600 g MNP per day (~28.3 L h^{-1}). The system operates at a residence time of approximately 4 min and 16 s, which is substantially shorter than the overall process durations typically reported for thermal decomposition syntheses (*e.g.*, several hours).[31] Its robust design minimizes clogging and fouling, thereby enhancing process efficiency and resource utilization. Due to the larger tube diameters, the millifluidic approach offers superior scalability and cost-efficiency, as it is easier and more economical to manufacture than micromixer-based systems.[39] Additionally, the system can facilitate real-time monitoring through the seamless integration of sensors, allowing precise control of synthesis parameters.[40] Furthermore, the modular system design allows easy integration of additional units, such as filtration or centrifugation modules. The Arduino®-based control system enables flexible tuning of parameters like flow rates and temperature, supporting the production of MNP with tailored properties. These advantages contribute to process intensification, making the system cost-efficient, sustainable and safe.

In the oxidative precipitation synthesis route applied in this study, a reduced metal precursor (Fe^{2+}) is employed, which is oxidized to Fe^{3+} during the precipitation process. This pathway can promote the formation of larger magnetite or maghemite cores.[41] Classical coprecipitation involves a rapid burst of nucleation, leading to a high number of nuclei and consequently limiting particle growth, which results in smaller nanoparticle sizes.[36] In contrast, synthesis routes that reduce the nucleation rate can provide more precursor per nucleus and thus promote the formation of larger particles. The oxidative precipitation synthesis route and its underlying reaction mechanisms have been investigated in previous studies, which provide comprehensive insights into intermediate phase formation, oxidation kinetics, and particle growth pathways.[42,43] Oxidative precipitation synthesis of MNP is governed by the base/OH^- concentration or pH, oxidant concentration, salt counterions, solvent composition, dissolved gas atmosphere, flow configuration, and complexing additives, which collectively affect particle size, morphology, surface charge, and magnetic properties.[43–46]

3 Materials and methods

The precursor concentrations for iron salt solution and base were selected based on a previously reported oxidative precipitation protocol.[42] To enable continuously driven MNP synthesis, 250 mL of deionized water were initially added for each of the three solutions (iron salt solution, base solution, and citric acid solution) and purged with nitrogen for at least 15 min. For the preparation of MNP, the iron salt solution was prepared by adding 3.6 g ferrous sulfate heptahydrate (Carl Roth GmbH + Co. KG, Ph. Eur., USP, purity ≥ 99.5%; 51.8 mmol L^{-1}), 0.4 g iron(III) chloride hexahydrate (Merck KGaA, ACS, Reag. Ph. Eur., for analysis; 5.9 mmol L^{-1}), and 0.2 mL sulfuric acid (Carl Roth GmbH + Co. KG, measured solution, 2.5 mol L^{-1}; 2.0 mmol L^{-1}). The base solution was prepared using 1.31 g potassium nitrate (Carl Roth GmbH + Co. KG, Ph. Eur., BP, purity ≥ 99%; 51.8 mmol L^{-1}) and 1.68 g sodium hydroxide (Carl Roth GmbH + Co. KG, p.a., ISO, purity ≥ 98%; 168 mmol L^{-1}). For the coating solution, 2.4 g citric acid (CA) (Carl Roth GmbH + Co. KG, p.a., ACS, anhydrous, ≥ 99.5%; 50.0 mmol L^{-1}) was added. Ammonia water (Merck KGaA, ISO, Reag. Ph. Eur., 25%, for analysis) and sulfuric acid (Carl Roth GmbH + Co. KG, measured solution, 2.5 mol L^{-1}, 5 N) were used for pH adjustment.

3.1. Synthesis of MNP

All solutions were purged with nitrogen for at least 15 min before usage and have a total volume of 250 mL each (iron salt solution, base solution, and CA solution). Per experiment, the iron salt liquid and base were pumped into the reactor at a rate of 2.6 mL s^{-1} (*cf.* Fig. 1). As soon as the first MNP emerge from the crystallization coil, the CA solution was pumped into the system *via* quenching unit. MNP were produced at different temperatures in the crystallization coil (indicated as reaction temperature) to characterize the process. The reactants contain 803.5 mg of iron in each experiment. The individual samples have the abbreviation 37MNP for a reaction temperature of 37 °C, the abbreviation 47MNP for a reaction temperature of 47 °C, and so forth up to 97MNP for a reaction temperature of 97 °C. The MNP prepared in this way were then stirred for one hour at pH 4. For scalability studies, mixing took place *via* magnetic stirrer, for all other experiments an electric impeller was used.

© 2026 The Author(s). Published by the Royal Society of Chemistry

Afterwards, the synthesis product was centrifuged at 3939*G* (4500 rpm) for 10 min. The resulting pellet was then dispersed in deionized water.

3.2. Characterization of MNP

The prepared MNP were analyzed by dynamic light scattering (DLS), electrophoretic light scattering (ELS), transmission electron microscopy (TEM) and superconducting quantum interference device (SQUID). Iron concentration of the MNP were determined by Fe^{3+} complexation, using Tiron as an indicator. Application specific properties for the MNP have been investigated for magnetic particle imaging (MPI), magnetic resonance imaging (MRI) and magnetic fluid hyperthermia (MFH).

3.2.1. Dynamic light scattering and zeta potential measurements. The measurements of hydrodynamic diameter and zeta potential were carried out using a Zetasizer Nano ZS (Malvern Instruments, Ltd, Worcestershire, UK). Each sample was shaken and diluted in deionized water for each measurement. DLS size measurements were performed three times at 20 °C. Zeta potential measurements were performed three times at 25 °C.

Mean hydrodynamic diameter of MNP, d_{hyd}, was derived from a fit with the log-normal distribution probability density function (PDF) to the diameters measured d using volumetric weighted data from the zetasizer:[47]

$$\mathrm{PDF}(d,\mu,\sigma) = \frac{1}{\sqrt{2\pi}\times d\times\sigma}\times \mathrm{e}^{-\frac{(\ln(d)-\mu)^2}{2\sigma^2}}. \quad (1)$$

The mean, d_{hyd} and variance, ${\sigma_{d_{\mathrm{hyd}}}}^2$, were determined using the fit parameters μ and σ with the expressions $d_{\mathrm{hyd}} = \mathrm{e}^{\left(\mu+\frac{\sigma^2}{2}\right)}$ and ${\sigma_{d_{\mathrm{hyd}}}}^2 = \mathrm{e}^{(2\mu+\sigma^2)}\times(\mathrm{e}^{(\sigma^2)}-1)$.

3.2.2. Transmission electron microscopy. A Hitachi TEM system (HT7800, Hitachi, Tokyo, Japan) at 100 kV was used to perform TEM measurements at the Institute of Pathology, Department of Electron Microscopy, University Hospital RWTH Aachen, Germany. The samples were pipetted on glow discharged grids (formvar carbon coated nickel grids, two hundred mesh, Electron Microscopy Sciences, Hatfield, PA, USA), excess liquid was drawn off and then dried. ImageJ software (version 1.54f) was used to determine the area of each MNP.[48] From this, the minimum (d_{min}) and maximum Feret diameters (d_{max}) were calculated (described as the longest and shortest distance between two points on the outer boundary of each nanoparticle that are opposed to each other).[49] The average size (d_{core}) is calculated *via* $d_{\mathrm{core}} = \frac{d_{\mathrm{max}}+d_{\mathrm{min}}}{2}$. The circularity of the samples is determined *via* $\frac{4\pi A_{\mathrm{area}}}{{U_{\mathrm{perimeter}}}^2}$ with A_{area} as surface area of the MNP and $U_{\mathrm{perimeter}}$ as MNP perimeter.[50] Log-normal cumulative distribution (CDF) was fitted to the data to obtain the mean and variance:

$$\mathrm{CDF}(d,\mu,\sigma) = \frac{1}{2}\times\left(1+\mathrm{erf}\left(\frac{\ln(d)-\mu}{\sqrt{2}\sigma}\right)\right) \quad (2)$$

with the parameters, μ and σ, from which the mean and variance are calculated with $d_{\mathrm{C}} = \mathrm{e}^{\left(\mu+\frac{\sigma^2}{2}\right)}$ and ${\sigma_{d_{\mathrm{C}}}}^2 = \mathrm{e}^{(2\mu+\sigma^2)}\times(\mathrm{e}^{(\sigma^2)}-1)$, respectively.

3.2.3. High resolution transmission electron microscopy. A Tecnai G2 F20 was used for high resolution transmission electron microscopy analysis. Dispersed CA coated MNP were dropped on a Cu–C-film grid. An acceleration voltage of 200 kV was used with a point-to-point resolution in ideal conditions of up to 1.4 Å. A bright field detector was used for HRTEM imaging. A description of the full methodology can be found in the SI.

3.2.4. Magnetic hyperthermia studies. Hyperthermia studies were performed in a custom-built facility (Trumpf Hüttinger GmbH + Co. KG, Freiburg, Germany) consisting of a water-cooled coil operating at a field amplitude $H = 40$ kA m^{-1} and a frequency $f = 270$ kHz, as well as $H = 19$ kA m^{-1} and $f = 95$ kHz. Samples were prepared with a volume of 1 mL in 4 mL flasks. Inside the flask, the temperature was measured with a fiber optic thermometer (Luxtron 812, LumaSense Inc., Santa Barbara, CA, USA). Water (as reference) as well as the samples were measured for 30 min. Subsequently, the data were used to determine the temperature difference. The iron concentration of the sample was 1 mg mL^{-1}. Resulting temperature data were fitted using the Box–Lucas function:

$$T(t) = T_{\mathrm{rise}}\times(1-\mathrm{e}^{(-bt)}) + T_0 \quad (3)$$

The fitting parameters were used to determine the specific loss power (SLP) according to:

$$\mathrm{SLP} = \frac{c}{\rho}\times\left.\frac{\mathrm{d}T}{\mathrm{d}t}\right|_{t\to 0}, \quad (4)$$

with the specific heat capacity of water, $c = 4.187$ J (g^{-1} K^{-1}), the MNP weight fraction, and $\left.\frac{\mathrm{d}T}{\mathrm{d}t}\right|_{t\to 0} = T_{\mathrm{rise}}\times b$, derived from the Box–Lucas fitting parameters.[51] The relation of iron mass to the total mass of the sample is denoted by ρ. In order to compare the heating power with other hyperthermia measurements, the intrinsic loss power (ILP) was calculated:[51]

$$\mathrm{ILP} = \frac{\mathrm{SLP}}{f\times H^2}. \quad (5)$$

3.2.5. Cytotoxicity assays. American Type Culture Collection (ATCC) fibroblast cell lines (L929) were cultured in RPMI 1640 (DMEM, Gibco, Invitrogen, USA) with 10% fetal bovine serum (FBS, Gibco, Invitrogen, USA) and 1% penicillin-streptomycin (Gibco, Invitrogen, USA) in humidified atmosphere with 5% CO_2 at 37 °C. CellTiter Glo® assay (Promega, Madison, USA) was used to determine cytotoxicity according to the supplier's instructions. In triplicate, L929 cells were seeded at a concentration of $c = 100\,000$ cells per mL and allowed to incubate with the synthesized MNP resp. Resovist® for 24 h. The tested iron concentrations were $c = [0, 10^0, 10^{0.5}, 10^1, 10^{1.5}, 10^2, 10^{2.5}, 10^3$ μg_{Fe} mL$^{-1}]$. For analysis of the effects of iron concentration c and MNP type on relative cell viability, a two-

© 2026 The Author(s). Published by the Royal Society of Chemistry

way ANOVA was performed in GraphPad Prism 9 (GraphPad Software, Inc., San Diego, USA) with Tukey's post hoc test ($\alpha = 0.05$). To compare the cytotoxicity of MNP, the EC_{50} value was determined using the Hill fit function:

$$CV_c = CV_{min} + \frac{CV_{max} - CV_{min}}{1 + \left(\frac{X}{EC_{50}}\right)^{n_H}}, \quad (6)$$

where CV_c is the relative cell viability, CV_{min} is the minimum relative cell viability and CV_{max} is the maximum relative cell viability. The parameter EC_{50} is the concentration that corresponds to the response at the halfway point between CV_{max} and CV_{min} and n_H is the Hill coefficient, that represents the slope of the fitting curve.[52]

3.2.6. Magnetic resonance measurements. Magnetic resonance measurements were performed using a clinical MRI scanner (3T Ingenia Elition, Philips Healthcare, The Netherlands) and a body coil. Samples were placed in a phantom containing polyacrylic acid and sodium chloride according to ASTM standards.[53] MNP samples were prepared with eight concentrations of iron ([Fe] = [0.025, 0.05, 0.075, 0.1, 0.125, 0.15, 0.175, 0.2] mM). For the study of transverse relaxivities (r_2), a Turbo Spin Echo (TSE) sequence (TR = 1500 ms, 32 echoes, TE = [6.05, 12.1, 18.15, … 193.7] ms, FOV = 366 × 366 mm, matrix 512 × 512, slice thickness 3 mm, flip angle 90°) was performed. For the study of longitudinal relaxivities (r_1) an inversion recovery spin echo (IRSE) sequence (repetition time TR = 5000 ms, 1 echo, echo time TE = 12 ms, inversion times TI = [50, 200, 400, 600, 800, 1000, 1200, 1400, 1600, 2000, 2500, 2900, 3300] ms, field of view FOV = 320 × 320 mm, matrix 256 × 256, slice thickness 5 mm, flip angle 90°) was performed. Transverse and longitudinal relaxivity $r_{1/2} = \frac{(R_{1/2} - R_{1.0/2.0})}{[Fe]}$, were calculated with R1/2 being the transverse relaxation rate of the MNP sample and R1.0/2.0 being the respective relaxation rate of the solvent. Relaxation rates of deionized water were used as reference.

3.2.7. Magnetic particle imaging. The system matrices for magnetic particle imaging were obtained using an MPI system (Bruker BioSpin® MRI GmbH, Ettlingen, Germany) equipped with a specialized 1D RX coil insert designed for mice, functioning as the receiver coil in the *x*-direction. Data were collected for system matrices consisting of 5 × 5 × 5 voxels with a field of view (FOV) of (6 × 6 × 6) mm^3. The iron concentration in the samples was 0.316 mg_{Fe} mL^{-1}, and all samples were contained in plastic capsules with a sample volume of 15.625 μL, provided by Bruker. In all spatial directions, the drive field amplitude was set at $B_{Drive} = 14$ mT, and the maximum gradient strength was $G_{max} = 2.5$ T m^{-1}. The system matrices were averaged 1000 times, and background correction was applied using measurements conducted during each individual acquisition of the system matrix. The signal-to-noise ratio (SNR) was calculated and plotted. To assess the decay of signal amplitude at higher harmonics, the ratio A_7/A_5 of the amplitudes of the 7th to the 5th harmonics was determined.

3.2.8. SQUID magnetometry. Magnetic properties of the samples were determined using an MPMS 5S superconducting quantum interference device (SQUID) magnetometer (LOT Quantum Design, San Diego, USA). Samples were prepared using 30 μL of MNP dispersion and 30 μL of 15% (w/w) mannitol solution mixed in a polycarbonate (PC) capsule and freeze-dried at −85 °C and 0.04 mbar for 12 h in a lyophilizer (Alpha 2-4 LDplus, Martin Christ Gefriertrocknungsanlagen GmbH, Osterode, Germany). Magnetization measurements were carried out at 295 K to determine the saturation magnetization values (M_s) normalized to the iron mass, varying the field strength between 4×10^6 A m^{-1} and $-4 \cdot 10^6$ A m^{-1} and again to 4×10^6 A m^{-1}. The Langevin function was fitted to the magnetization data:

$$L(\xi) = \coth(\xi) - \frac{1}{\xi}, \quad (7)$$

with $\xi = \frac{\mu H}{k_B T}$, the MNP magnetic moment $\mu = V_M M_S$ and the MNP volume V_M, the applied magnetic field H and the Boltzmann constant $k_B = 1.38 \times 10^{-23}$ J K^{-1}. The magnetic particle diameter d_m was determined by Chantrell fitting assuming log-normal distributed MNP sizes.[54,55]

4 Results and discussion

To produce MNP with optimized performance for MFH, MRI and MPI (Section 2), a continuous millifluidic synthesis method was developed. For this, the reaction temperature, a key factor influencing MNP properties,[29] was varied between 47 °C and 97 °C. Samples are denoted according to the used reaction temperatures (*cf.* Table 1). MNP size and iron yield were

Table 1 Summary of the results of the TEM, DLS and yield analysis: core diameter (d_{core}), circularity of MNP-cores, hydrodynamic diameter (d_{hyd}) and yield. Core and volume-weighted hydrodynamic diameters were determined with a fit to the cumulative distribution respectively probability density function of a log-normal distribution (*cf.* Fig. S4). The distribution of MNP core diameters with a fit of the cumulative distribution function is shown in Fig. S8

Acronym↓/property→	d_{core}/(nm)	Circularity/(−)	d_{hyd}/(nm)	Yield/(%)
47MNP	17.5 ± 4.2	0.96 ± 0.02	212.9 ± 97.9	10.0 ± 0.1
57MNP	18.7 ± 3.6	0.95 ± 0.02	118.6 ± 93.0	11.7 ± 0.2
67MNP	23.5 ± 4.6	0.96 ± 0.02	57.6 ± 30.2	73.7 ± 12.2
77MNP	20.8 ± 4.3	0.97 ± 0.02	84.0 ± 36.8	92.3 ± 4.4
87MNP	21.7 ± 3.9	0.96 ± 0.02	65.6 ± 32.3	48.5 ± 3.4
97MNP	27.3 ± 4.2	0.97 ± 0.02	79.41 ± 32.8	42.9 ± 1.5

© 2026 The Author(s). Published by the Royal Society of Chemistry

analyzed *via* DLS, TEM, and photometry to calculate iron concentration (*cf.* Materials and methods). TEM analysis shows an increasing core size with rising temperature (Fig. 2A–F). The smallest core diameters were obtained with 47MNP (17.5 ± 4.2 nm). 47MNP shows (Fig. 2A), both rod-shaped and spherical MNP, while sample 57MNP (Fig. 2B) shows only spherical MNP.

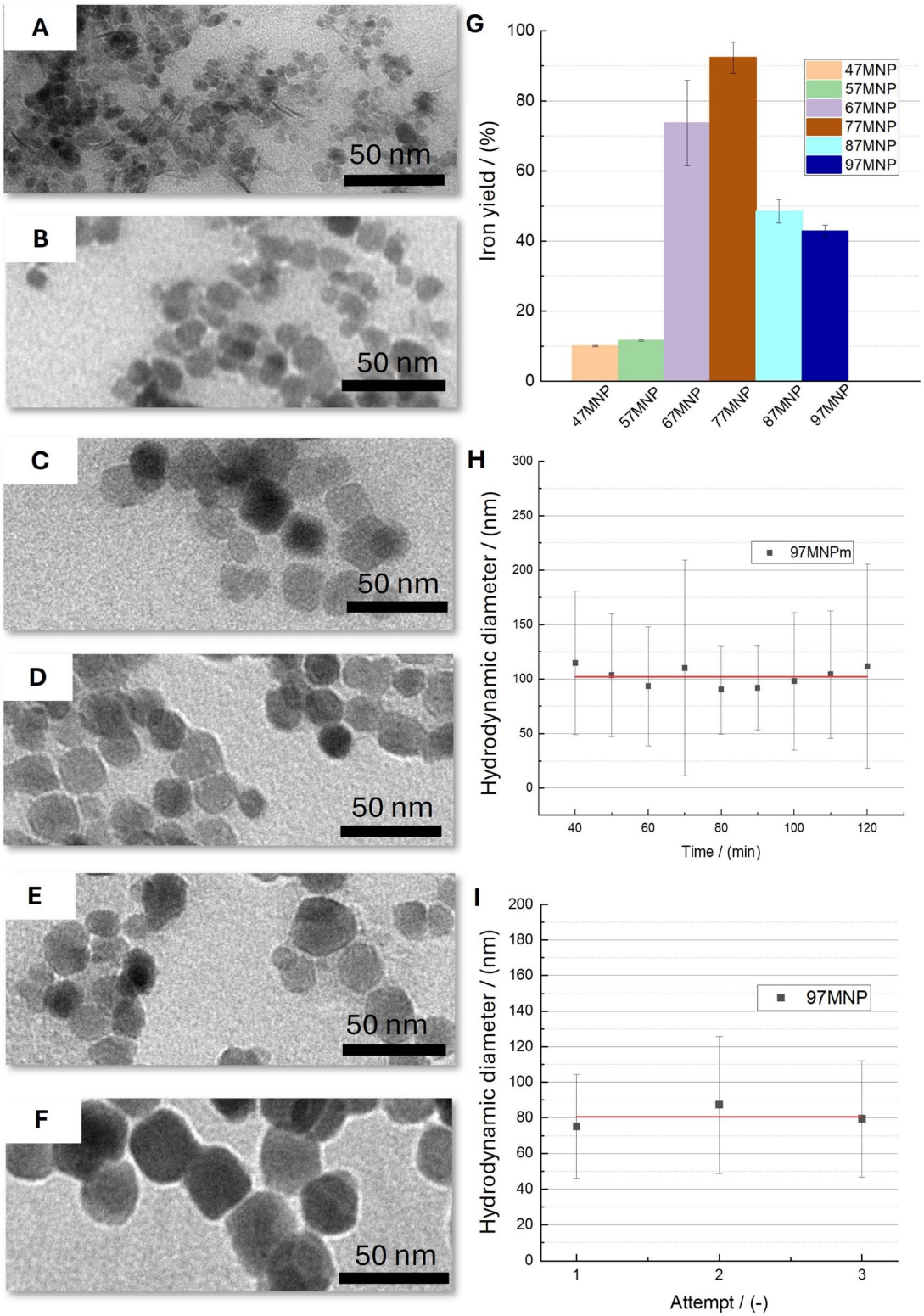


Fig. 2 Exemplary TEM images of MNP synthesized at (A) 47 °C, (B) 57 °C, (C) 67 °C, (D) 77 °C, (E) 87 °C, (F) 97 °C. The core diameters are listed in Table 1. (G) Iron yield of synthesized samples at temperatures between 47 °C and 97 °C. (H) Hydrodynamic diameter of MNP measured every 10 min, error bars represent the standard deviation. (I) Hydrodynamic diameter of MNP measured over three independent attempts. Error bars represent the standard deviation of three independent measurements.

© 2026 The Author(s). Published by the Royal Society of Chemistry

Table 2 Intrinsic loss power (ILP), specific loss power (SLP), maximum temperature difference to room temperature (ΔT_{max}), longitudinal and transversal relaxivity (r_1 and r_2), ratio between the 7th and 5th harmonic amplitude in MPI (A_7/A_5), EC_{50}-value (EC_{50}), zeta-potential (ζ), magnetic susceptibility (χ) and magnetic saturation (M_s) are presented

Symbol/unit	Resovist®	77MNP	97MNP
ILP/(nHm^2 kg^{-1})			
@$H = 40$ kA m^{-1}, $f = 270$ kHz	0.69 ± 0.10	1.95 ± 0.29	2.78 ± 0.41
@$H = 19$ kA m^{-1}, $f = 95$ kHz	—	5.1 ± 0.20	5.4 ± 0.26
SLP/(W g_{Fe}^{-1})			
@$H = 40$ kA m^{-1}, $f = 270$ kHz	297.0 ± 33.0	939.3 ± 42.2	1337.1 ± 59.4
@$H = 19$ kA m^{-1}, $f = 95$ kHz	—	171.4 ± 9.4	186.0 ± 9.1
ΔT_{max}/(°C)			
@$H = 40$ kA m^{-1}, $f = 270$ kHz	18.2 ± 0.2	42.12 ± 0.2	50.6 ± 0.2
@$H = 19$ kA m^{-1}, $f = 95$ kHz	—	15.4 ± 0.6	15.8 ± 0.4
r_2/(1/mMs)	186.96 ± 4.42	528.72 ± 10.2	480.57 ± 8.31
r_1/(1/mMs)	5.7 ± 0.2	5.82 ± 0.19	16.64 ± 0.85
A_7/A_5(−)	0.32	0.16	0.16
EC_{50}/(%)	294.8 ± 3.7	147.4 ± 42.5	188.2 ± 25.6
ζ-Potential/(mV)	−25.3 (ref. 70)	−45.2	−50.4
X/(−)	—	9.1 ± 0.2	8.4 ± 0.1
M_s/(Am^2 kg^{-1})	101.6 ± 12.2 (ref. 32)	101.3 ± 0.5	87.0 ± 0.2

An increase in size of 56% was observed by increasing the temperature (*cf.* diameters size of 57MNP and 97MNP, Fig. 2B–F). DLS data indicate small hydrodynamic diameters and reduced standard deviations at higher temperatures (Table 2). Circularity analysis confirms high uniformity (*e.g.*, (0.96 ± 0.02) for 77MNP, (0.97 ± 0.015) for 97MNP), which potentially enhances magnetic field response. MNP formation follows oxidation pathways influenced by OH^- excess, pH, and Fe^{2+}/Fe^{3+} ratio.[56,57] Rod-like structures likely represent precursors such as akaganeite or goethite.[58–61] Rapid base-iron salt mixing favors magnetite formation *via* iron hydroxides and lepidocrocite.[56] A residence time that is long enough promotes the full conversion to magnetite, while the addition of CA selectively removes the unwanted phases.[56] Higher reaction temperatures seem to accelerate crystallization, leading to larger core sizes,[62] while CA quenching stabilizes MNP and reduces hydrodynamic diameter.[33,56,63] The millifluidic closed system prevents oxidation, ensuring phase control. The larger core diameters observed for sample 97MNP may additionally result from the combination of quenching at elevated temperature and the subsequent centrifugation step. Quenching with CA at high temperature can lead to smaller hydrodynamic diameters,[33] which may correspond to smaller MNP cores. During the subsequent centrifugation step, these smaller particles may remain in the supernatant and thus be partially removed from the final product. Size-selective modifications induced by centrifugation have previously been reported in the literature.[64] Iron yield serves as an indicator of production scalability. At 47–57 °C, yields are low ((11.7 ± 0.2) %). Between 57 °C and 77 °C, the yield increases sharply to (92.3 ± 4.4) % but declines at 87 °C ((48.5 ± 3.4) %) and 97 °C ((42.9 ± 1.6) %) (Fig. 2G). The lower yield at high temperatures can be attributed to smaller hydrodynamic diameters, causing increased loss during centrifugation. A potential daily iron production reaches ∼676 g for 77MNP. The estimated cost per gram (only educts) is < 1.2 €/g_{Fe} for 97MNP and < 0.53 €/g_{Fe} for 77MNP, with production rates of 12.9 g_{Fe} h^{-1} and 27.8 g_{Fe} h^{-1}, respectively.

To evaluate the scalability of the continuous synthesis, a 120 min long-term run was performed to demonstrate sustained reactor operation over extended process time. Here, the influence of process time on the d_{hyd} of the MNP was investigated. Samples were taken from the modular MNP synthesis process every 10 min in a time range between 40 and 120 min and subsequently analyzed *via* DLS. The corresponding volume-weighted size distributions of the d_{hyd} with a fit to the PDF of the log-normal distribution are displayed in Fig. S6 in the SI. The results show MNP d_{hyd} between 90.22 nm and 114.69 nm. The diameter difference between the average of all recorded values between 40 and 120 min (102.03 nm) and the one at a specific timepoint in the production line was calculated to evaluate the stability of the process. The largest differences occurred at 40 min (12.41 nm) and 80 min (11.58 nm), while the smallest differences were measured at 50 min (1.48 nm) and 110 min (2.17 nm). The average difference over all time points was 7.47 nm. Larger differences between MNP size that occurred at 40 min and 80 min may be due to the manual handling of the downstream process. In comparison to reproducibility (Fig. 2I) and performance tests (Fig. 4) magnetic stirrers were used for scalability studies, which could explain the different d_{hyd}. Larger differences in MNP size observed at 40 min and 80 min may be attributed to manual handling during downstream processing, which currently represents a limitation for fully continuous large-scale operation and may introduce variability during particle separation, washing, and sample collection. In particular centrifugation is presently performed in batch mode and limited to comparatively small

© 2026 The Author(s). Published by the Royal Society of Chemistry

processing volumes (~200 mL per run), which may constrain further scale-up unless continuous separation strategies are implemented. Future work will further focus on automating the downstream process to further minimize manual handling and increase process reliability.

Reproducibility studies confirm the stability of the synthesis process: three independent synthesis under identical process conditions yielded in a d_{hyd} of (75.2 ± 29.0) nm, (79.4 ± 32.8) nm, and (87.3 ± 38.4) nm. The corresponding volume-weighted size distributions of the hydrodynamic diameters with a fit to the PDF of a log-normal distribution the reproducibility study are displayed in Fig. S5 in the SI. The mean value of all approaches was (80.6 ± 33.4) nm, which means that the results are scattered in a narrow range around the mean value (Fig. 2I). Taken together, the findings support the conclusion that the synthesis process offers scalability, cost-efficiency, and operational robustness. The process needs further optimization, especially by automation of downstream operations, to achieve tighter reproducibility.

4.1. Application specific MNP analysis

Samples 77MNP and 97MNP were selected for further analysis due to their high yield (77MNP) and tailored core sizes with a narrow size distribution (97MNP) for hyperthermia and magnet-based imaging.[65,66] Their crystallographic structure and magnetization properties were investigated using a high-resolution transmission electron microscope (HRTEM, Fig. 3D–I) and a superconducting quantum interference device (SQUID, Fig. 4A). Selected area electron diffraction (SAED, Fig. 3A–C) was performed to verify phase composition and

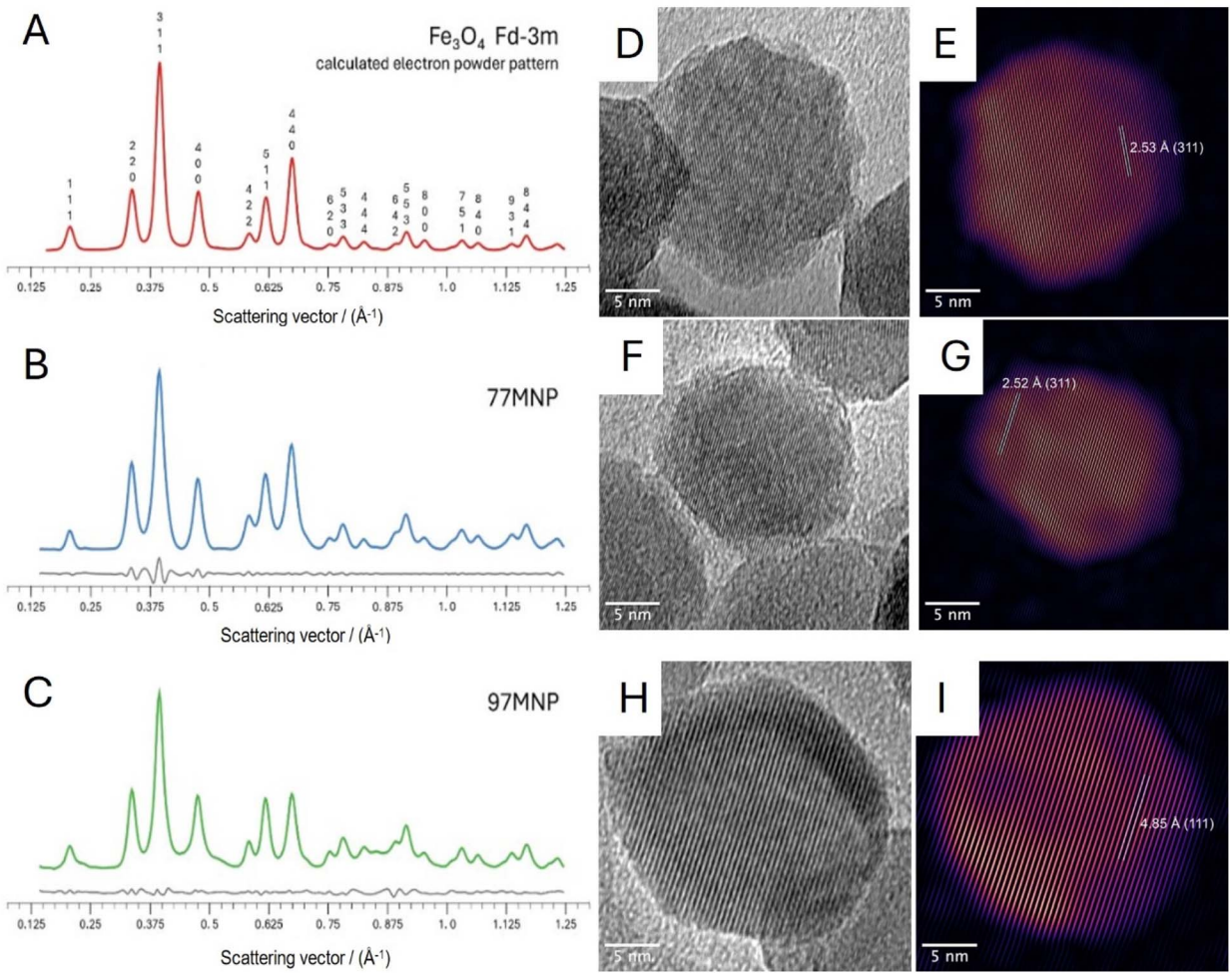


Fig. 3 (A) Calculated electron powder profile of spinel-type Fe_3O_4 using the program FULLPROF 63. (B) and (C) Modelled experimental diffraction profiles for 97MNP and 77MNP (*cf.* SI section for details). The shown curves in grey colour represent the difference between the shown model curves and the pseudo-powder diffraction pattern that was obtained from three SAED patterns each. Visual comparison of the three profiles supports that the synthesised nanocrystalline materials are almost pure magnetite in both cases. (D) and (F) HRTEM image of typical nanocrystals in sample 77MNP. (E) and (G) Corresponding Fourier lattice filtered image showing the 311 planes of the magnetite structure. As for sample 97MNP also these nanocrystals are virtually free of defects and faults, which is required for superior magnetic performance. (H) HRTEM image of a typical nanocrystal in sample 97MNP. (I) Corresponding Fourier lattice filtered image showing the 111 planes of the magnetite structure. As judged from the undistorted planes through this nanocrystal, this particle does not contain a significant number of faults. However, the notable small bending of the planes at the outer rim and contrast differences within the crystal might indicate some residual stress.

© 2026 The Author(s). Published by the Royal Society of Chemistry

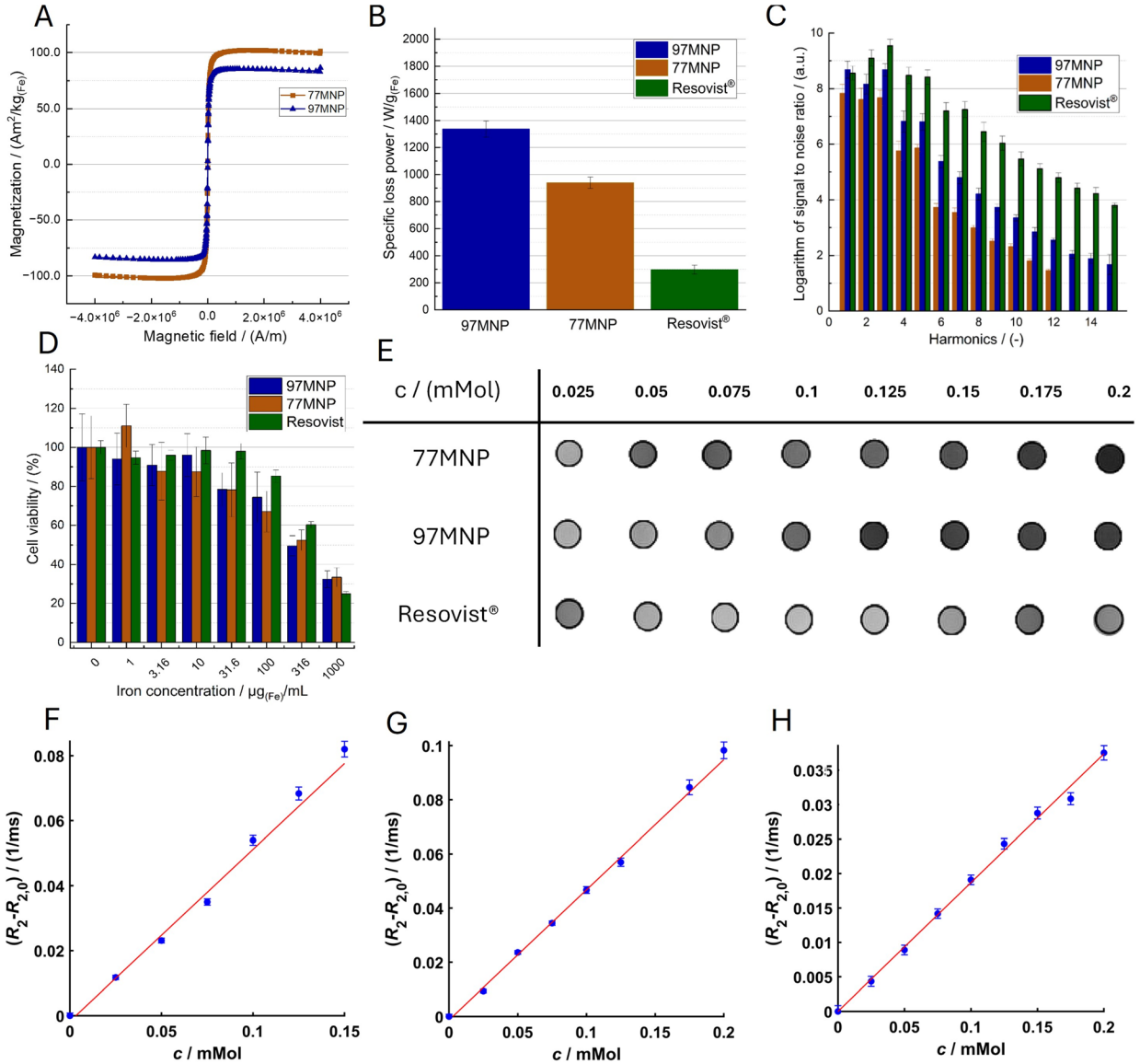


Fig. 4 (A) Magnetization value with a fit of the Langevin function (*cf.* eqn (7)) for the sample 97MNP and 77MNP. (B) Bar chart showing SLP values for 97MNP, 77MNP and Resovist® samples. (C) Signal to noise ratio (SNR) *vs.* harmonic number for MNP samples 97MNP, 77MNP and Resovist® up to the 15th harmonic. (D) Cytotoxicity analysis of self-synthesized MNP and Resovist®. Cytotoxicity analysis was performed with L929 mouse fibroblasts. R_0 denotes the relaxation rate value of the reference sample without MNP. (E) Exemplary T_2-weighted MRI images for MNP at selected iron concentrations for the MNP samples in (F)–(H). (F–H) R_2 relaxation rates *vs.* iron concentration with linear fit for (E) 77MNP, (F) 97MNP and (G) Resovist®.

determine the lattice parameters. Due to the limited number of nanocrystallites within the SAED field aperture, the obtained ring patterns were incomplete (Fig. S1 and S2) and unsuitable for precise interplanar spacing analysis. Instead, pseudo-powder diffraction profiles were generated (Fig. 3B and C) based on three SAED patterns per sample. Initial analysis indicates agreement with spinel-type Fe_3O_4 ($a \approx 8.4$ Å, space group $Fd\bar{3}m$ #227). A simulated electron powder diffraction pattern (FULLPROF[67]) confirmed the close match between experimental and theoretical profiles (Fig. 3A). Lattice parameters were determined *via* full-pattern LeBail fitting,[68] yielding $a = 8.405(10)$ Å for 97MNP and $a = 8.402(2)$ Å for 77MNP. A secondary refinement approach using manually determined peak positions provided $a = 8.401(2)$ Å (97MNP) and $a = 8.393(2)$ Å (77MNP). Experimental details are provided in the SI section (pages S1–S11). HRTEM analysis indicates the high crystallinity and structural quality of both samples. The surface of 77MNP appears rougher than 97MNP (*cf.* Fig. 3D and H) likely due to higher susceptibility to CA treatment. This could result from a larger surface-to-volume ratio, exposing more surface area to CA. Literature reports indicate op to 8% reduction in MNP size due to surface ablation by CA.[56] While thermal decomposition yields defect-free MNP with high saturation magnetization, it requires toxic organic solvents and long

© 2026 The Author(s). Published by the Royal Society of Chemistry

synthesis times (up to 40 h), making precipitation-based synthesis an efficient alternative for high scale production. Diffraction methods cannot distinguish magnetite (Fe_3O_4) from its oxidized counterpart maghemite (γ-Fe_2O_3).[69] Here, magnetite was assumed as the dominant phase. Both samples exhibited uniform, undistorted crystal structures, indicating single-domain particles, consistent with expectations for magnetite MNP below (20–30) nm.[70] Saturation magnetization is influenced among others by the iron oxide phase, core size, crystal structure, and surface coating.[71] It serves as an indicator of crystallographic changes and synthesis quality. Fig. 4A displays the magnetization curves of sample 77MNP and 97MNP. Sample 77MNP exhibits the highest saturation magnetization, followed by Resovist®[32] and 97MNP, *cf.* Table 2. In comparison, bulk magnetization of magnetite is 127 $Am^2 kg^{-1}$.[72] The high magnetization of 77MNP and 97MNP is attributed to their high crystallinity and the absence of structural disorder (Fig. 4A). Magnetite has the highest bulk magnetization among iron oxides, surpassing maghemite and non-magnetic phases such as wustite.[73] As the direct coating in the continuous process prevents oxidation, influences on magnetization are expected to come from MNP size.

In general, magnetization was shown to increase with core size in the 1–10 nm range,[74] however, for larger MNP, multi-domain splitting may occur leading to lower magnetization values. The latter explains the lower magnetization value for 97MNP compared to the one of 77MNP. Continuously operated microfluidic systems produce MNP with similarly high saturation magnetizations.[46] Stirred tank reactors in series for ageing/oxidation to magnetite under continuous flow conditions reach slightly lower M_s-values.[43] The SLP and ILP of 77MNP, 97MNP and, as reference, of Resovist® (Fig. 4B and Table 2) were determined to estimate their hyperthermia performance (*cf.* Chapter 3.2.4). The SLP of 97MNP is 4.5 times higher than that of Resovist® and the maximum temperature difference is about 2.8 times higher. High SLP values are advantageous for MFH, particularly for systemic applications of MNP reaching low concentrations at target sites.[75] For high SLP values, the interplay between field parameters (amplitude H, frequency f) and MNP properties, including core size, hydrodynamic diameter, agglomeration, and magnetization plays is key.[76] Heat generation occurs *via* Néel and Brownian relaxation. Larger MNP undergo a transition from Brownian-to Néel-dominated relaxation,[77] with 77MNP and 97MNP expected to be Brownian dominated.[78] Field amplitude and magnetic anisotropy influence relaxation, necessitating combined Néel–Brownian modeling to optimize heating efficiency.[79] Interparticle interactions also affect heating performance, influencing the collective magnetic response. For the different applied magnetic fields, the ILP values show a deviation. The ILP formalism is primarily applicable at low magnetic field amplitudes, where the SLP follows the expected quadratic dependence on the applied field strength.[80,81] As the field amplitude increases, however, this quadratic behaviour progressively breaks down and the SLP-field relation transitions toward a linear regime. Consequently, ILP values decrease at higher field amplitudes, not because the material becomes intrinsically less efficient, but because the ILP definition itself assumes a quadratic dependence that no longer holds under these conditions. This highlights an important conceptual limitation of ILP: while it is useful for comparing materials under standardized low-field conditions, it should not be interpreted as a universal measure across the full range of experimentally relevant field strengths. In practical hyperthermia applications, where higher fields are often employed, the SLP itself provides a more direct and physically meaningful measure of heating performance.

The role of the above-mentioned parameters and properties on SLP was investigated in many studies. For example, it was shown that MNP with high magnetic anisotropy and non-spherical shapes (*e.g.*, cubes, rods) exhibit enhanced heating efficiency.[82,83] The core sizes of 77MNP and 97MNP align with optimal values (~20 nm) for efficient heat generation.[29,84,85] SLP shows a tendency to increase with increasing core diameter, although the effect is less pronounced for larger MNP core sizes from around 25 nm.[86] Spherical MNP agglomeration lead to a reduction of heating output.[87,88] This might also influence the heating output of 77MNP, as agglomerations are indicated by the difference between core and hydrodynamic size (Table 2).

HRTEM and diffraction data confirm a defect-free magnetite crystal structure in both samples (Fig. 3), contributing to high magnetization and heating performance.[89] CA coating induces a magnetically frustrated layer, affecting smaller MNP more strongly [90] which could explain the lower heating output of 77MNP. Also, MNP core sizes at the boundary between single-domain and multi-domain can lead to high heating capacities [57] which is the case for 97MNP. ILP values (97MNP: (5.4 ± 0.26 $nHm^2 kg^{-1}$)) are higher than commercially available MNP.[81] 97MNP and 77MNP at a concentration of 1 mg mL^{-1}, ($f = 95$ kHz and $H = 19$ kA m^{-1}), achieve a substantial therapeutic temperature increase ($\Delta T > 15$ °C, *cf.* Fig. S9 in the SI) while remaining within the acceptable safety limit of $H \cdot f \leq 5 \times 10^9$ A m^{-1} s^{-1}.[91] Considering that a temperature increase of ~6–8 °C is sufficient to achieve therapeutic efficacy in hyperthermic cancer treatment, this provides a substantial level to reduce either MNP concentration or field parameters to minimize potential adverse effects in patients.[92] Magnetic nanoflowers exhibit higher ILP (up to 8.4 $nHm^2 kg^{-1}$),[93] but their synthesis is complex and difficult to scale. Alternative strategies, including doping with Zn or Mg and shape tailoring, have been explored to enhance heating efficiency.[83,94,95]

77MNP and 97MNP were evaluated as contrast agents and compared to FDA-approved contrast agent Resovist®. Higher r_2-values enhance negative contrast. The MNP in this work have r_2-relaxivity values up to 2.8 times higher than the ones of Resovist® (Fig. 4F and G). In general, r_2 is influenced by magnetic susceptibility, core size, and agglomeration.[96,97] Measurement settings and MRI field strength also play an important role.[98] The high r_2-values of 77MNP and 97MNP can be explained by their high magnetic susceptibility and crystallinity (Fig. 3, Section 3).

r_1-Values, determining positive contrast potential, were also measured (Fig. S7). The r_2/r_1 ratio defines the contrast type, with higher values for negative contrast.[99] For 97MNP, $r_2/r_1 = 28.9$,

© 2026 The Author(s). Published by the Royal Society of Chemistry

and for 77MNP, $r_2/r_1 = 90.8$, a strong negative contrast effect is expected, surpassing literature-reported values.[100–102] In comparison, hydrothermal-synthesized magnetite nanorods exhibit 13% higher r_2, but the synthesis requires the use of toxic solvents, high temperatures (200 °C), and long synthesis durations, limiting industrial applicability.[103]

MPI performance was assessed by measuring signal-to-noise ratios (SNR) up to the 15th harmonic (Fig. 4C). The amplitude decay ratio A_7/A_5, a key quality parameter, was evaluated. Although MNP with ~27 nm core sizes were reported to be optimal for MPI,[104] 77MNP and 97MNP exhibited A_7/A_5 ratios ~50% lower than expected, suggesting suboptimal MPI response compared to Resovist®. As MPI and hyperthermia are both based on the non-linear dynamic magnetic susceptibility, the relaxation dynamics play a crucial role in reaching high performance. Further, particle interactions strongly influence MPI signals, as observed for aggregated MNP.[105] Improved understanding of relaxation mechanisms and further optimization of MNP properties are necessary to create high-performance MPI tracers.[85]

All samples, 77MNP, 97MNP (CA-coated), and Resovist® (dextran-coated), were tested for cytotoxicity (Fig. 4D). Cell viability decreases with increasing iron concentration, with significant differences observed at 31.62 $\mu g_{Fe}\,mL^{-1}$. At 1000 $\mu g_{Fe}\,mL^{-1}$, viability sharply decreases. There are many possible factors: A major influence on cell viability is the amount of internalized MNP. MNP uptake occurs *via* phagocytosis and endocytosis, influenced by hydrodynamic diameter, surface charge, aggregation, and stability in biological media.[106,107] Internalization kinetics must be assessed for each MNP type.[108–110] Negatively charged CA-coated MNP exhibit up to three times higher cellular uptake than dextran-coated MNP, explaining lower cell viability (*cf.* zeta potential in Table 2).[111,112] Faster degradation of CA-coated MNP further contributes to cytotoxicity differences.[113] Surfactants influence imaging performance. Biocompatible coatings such as dextran, polyethylene glycol, and CA improve stability and circulation time.[73,96] Thus, CA-coated MNP offer advantages for functionalization in biomedical applications, including drug delivery.[114] Clinical trials confirm sufficient blood circulation half-lives for CA-coated MNP.[96,115,116] Manufacturing processes significantly affect MNP purity, impacting cytotoxicity. Thus, higher purity can be achieved through dialysis, filtration, magnetic separation, and centrifugation, removing excess coating agents, synthesis byproducts, and ions, thereby reducing toxicity.[117]

4.2. Application prospects and current limitations

Clinical translation of MNP therapies depends on the reproducibility, scalability, and efficacy of MNP production. Further, extensive characterization is required to establish MNP as viable diagnostic and therapeutic agents. This study focuses on optimizing MNP production, emphasizing high-yield and cost-effective synthesis (*cf.* production yield analysis in Section 3). The millifluidic system enables controlled, standardized, and reproducible MNP synthesis, crucial for medical applications. Specifically, CA-coated MNP offer functionalization potential *via* carboxyl groups on the MNP surface, facilitating covalent binding to biomolecules such as proteins, antibodies, or drugs.[63] Further system optimizations are necessary, including refining hydrodynamic size distributions through flow rate adjustments, increasing saturation magnetization *via* alternative reactant compositions, and enhancing yield by optimizing reactant concentrations. Long-term stability studies are essential to assess storage capabilities under different conditions. Advanced characterization techniques, such as Fourier transform infrared spectroscopy, dynamic magnetic susceptibility, thermogravimetric analysis, X-ray photoelectron spectroscopy, Raman spectroscopy, and Mössbauer spectroscopy, could provide deeper insights into MNP chemical and magnetic properties.[118] For clinical applications, *in vitro* cell studies must be followed by *in vivo* animal models and, eventually, human trials.[119]

The high r_2-values make the synthesized MNP promising as negative MRI contrast agents, suitable for early detection of tumors, inflammation, and other pathological changes.[120] As an example, MNP have been explored and are of high relevance in diagnosis for neuro-oncology and central nervous system diseases.[121] The demand for alternative contrast agents is driven by concerns over gadolinium (Gd)-based agents, which exhibit short circulation times and toxic Gd ion release, particularly in patients with renal impairment.[122,123] Additionally, Gd accumulation in brain tissue raises safety concerns,[124] reinforcing the need for safer MNP-based MRI agents. There is growing interest in novel agents for advanced diagnostic applications, such as tumor imaging in combination with immune cell tracking.[125]

The versatility of the millifluidic system could facilitate MNP production for applications such as magnetic cell separation, MPI, and T_1-weighted MRI contrast agents. Combining the continuously driven, modular, millifluidic flow system presented here with in-line measurement methods and AI-driven decision-making[126,127] could make it possible to implement a self-driving laboratory. Thanks to continuous flow, this lab could conduct more experiments and create more controlled environments than batch approaches.[128,129] Integrating advanced analytical methods is crucial for generating training data and ensuring product quality.[130] These advancements could enhance synthesis efficiency, reduce errors, and improve reproducibility, paving the way for scalable and clinically viable MNP applications.

Beyond diagnostics, MNP offer various therapeutic applications, including MFH, which selectively destroys tumor cells while minimizing damage to healthy tissue. MFH can also enhance drug delivery by enabling thermally controlled drug release.[131] MNP-functionalized biodegradable scaffolds have been investigated for bone tumor therapy,[132,133] and MNP-embedded implants allow MRI-based position monitoring and MFH-based tumor treatment in hollow organs.[82,134] The combination of imaging and therapy enables image-guided interventions, with MPI-MFH fusion allowing real-time targeted heating. Custom-built MPI-MFH devices have been developed for MNP localization and controlled heating.[135,136] MPI has potential for *in vivo* cancer imaging, cardiovascular imaging, acute stroke detection, and stem cell tracking.[137,138]

© 2026 The Author(s). Published by the Royal Society of Chemistry

5 Conclusion

The presented production process is based on a continuous, modular, and scalable millifluidic oxidative precipitation approach, enabling precise control over mixing and reaction conditions, followed by controlled quenching and functionalization. With this system fast mixing times (τ_{mix} << 10 ms) at the beginning of the reaction and high production rates (28.3 L h^{-1}) can be achieved. Overall important synthesis parameters (*e.g.* mixing conditions and reaction temperature) can be adjusted precisely and independently, as all components controlling the synthesis are modularly integrated. Due to the millifluidic production method, clogging is avoided. As the synthesis is performed in an aqueous environment, a low environmental impact and low costs are expected. By varying the reaction temperature, the size of the MNP can be tailored in the range of 17 nm-27 nm. The core size of the MNP is important for a wide range of applications and can be customized with the system for specific applications. It was demonstrated that the MNP are promising for various biomedical applications, such as contrast and hyperthermia agents as well as tracers. The 97MNP reached an ILP value of (5.4 ± 0.26) nHm^2 kg^{-1}, which is higher than commercially available stable MNP.[81,139] For 77MNP, an r_2-value of (528.7 ± 10.2) 1/mMs was achieved, showing favorable properties as contrast agents in MRI. The EC_{50}-value of up to (188.2 ± 25.6) μg_{Fe} mL^{-1} for 97MNP is in accordance with the typical one for CA-coated MNP. The production line presented in this work combines high throughput with precise control of synthesis parameter enabling the production of MNP with high particle performance in hyperthermia and imaging.

Further automatization and optimization of the production system are envisioned by adding a continuous separation of MNP, *e.g.* by continuous centrifugation, crossflow filtration or field flow fractionation. *In situ* measurement techniques (magnetic sensors or diffraction techniques) can be used to track MNP properties during the synthesis and possibly develop prediction models for MNP properties.

Conflicts of interest

The author(s) report no conflicts of interest in this work.

Data availability

The authors confirm that the data supporting the findings of this study are available within the article and its supplementary information (SI). Supplementary information is available. See DOI: https://doi.org/10.1039/d6na00187d.

Raw research data is available upon request.

Acknowledgements

We gratefully acknowledge financial support by the German Research Foundation (grant no. 467959793), and by the Federal Ministry of Education and Research (grant no. 03VP10973). We gratefully acknowledge the financial support by the by the European Union (ERC, MAD Control, 101076174). Views and opinions expressed are however those of the author(s) only and do not necessarily reflect those of the European Union or the European Research Council Executive Agency. Neither the European Union nor the granting authority can be held responsible for them.

References

1 G. G. Flores-Rojas, F. López-Saucedo, R. Vera-Graziano, E. Mendizabal and E. Bucio, Magnetic Nanoparticles for Medical Applications: Updated Review, *Macromol*, 2022, **2**, 374–390.

2 N. Kumar, P. Chamoli, M. Misra, M. K. Manoj and A. Sharma, Advanced metal and carbon nanostructures for medical, drug delivery and bio-imaging applications, *Nanoscale*, 2022, **14**, 3987–4017.

3 M. G. M. Schneider, M. J. Martín, J. Otarola, E. Vakarelska, V. Simeonov, V. Lassalle and M. Nedyalkova, Biomedical Applications of Iron Oxide Nanoparticles: Current Insights Progress and Perspectives, *Pharmaceutics*, 2022, **14**, 204.

4 T. I. Shabatina, O. I. Vernaya, V. P. Shabatin and M. Y. Melnikov, Magnetic Nanoparticles for Biomedical Purposes: Modern Trends and Prospects, *Magnetochemistry*, 2020, **6**, 30.

5 A. Dasari, J. Xue and S. Deb, Magnetic Nanoparticles in Bone Tissue Engineering, *Nanomaterials*, 2022, **12**, 757.

6 B. Mues, B. Bauer, A. A. Roeth, J. Ortega, E. M. Buhl, P. Radon, F. Wiekhorst, T. Gries, T. Schmitz-Rode and I. Slabu, Nanomagnetic Actuation of Hybrid Stents for Hyperthermia Treatment of Hollow Organ Tumors, *Nanomaterials*, 2021, **11**, 618.

7 A. I. Gonçalves, M. T. Rodrigues, P. P. Carvalho, M. Bañobre-López, E. Paz, P. Freitas and M. E. Gomes, Exploring the Potential of Starch/Polycaprolactone Aligned Magnetic Responsive Scaffolds for Tendon Regeneration, *Adv. Healthcare Mater.*, 2016, **5**, 213–222.

8 R. P. Friedrich, I. Cicha and C. Alexiou, Iron Oxide Nanoparticles in Regenerative Medicine and Tissue Engineering, *Nanomaterials*, 2021, **11**, 2337.

9 Y.-X. J. Wang, Superparamagnetic iron oxide based MRI contrast agents: Current status of clinical application, *Quant. Imaging Med. Surg.*, 2011, **1**, 35–40.

10 B. Thiesen and A. Jordan, *Clinical Applications of Magnetic Nanoparticles for Hyperthermia, International Journal of Hyperthermia : the Official Journal of European Society for Hyperthermic Oncology*, North American Hyperthermia Group, 2008, vol. 24, pp. 467–474.

11 V. Hartung, J. Günther, A. M. Augustin, T. Reichl, P. Gruschwitz, M. A. Rückert, T. A. Bley, V. C. Behr, S. Herz and P. Vogel, Resotran® meets MPI – clinically approved Ferucarbotran reintroduced: a major leap towards MPI in humans, *Int. J. Magn. Part. Imaging*, 2023, **9**, 2303058.

12 D. D. Stueber, J. Villanova, I. Aponte, Z. Xiao and V. L. Colvin, Magnetic nanoparticles in biology and medicine: past, present, and future trends, *Pharmaceutics*, 2021, **13**, 943.

 © 2026 The Author(s). Published by the Royal Society of Chemistry

13 A. Russo, M. Bianchi, M. Sartori, M. Boi, G. Giavaresi, D. M. Salter, M. Jelic, M. C. Maltarello, A. Ortolani, S. Sprio, M. Fini, A. Tampieri and M. Marcacci, Bone regeneration in a rabbit critical femoral defect by means of magnetic hydroxyapatite macroporous scaffolds, *J. Biomed. Mater. Res. Part B Appl. Biomater.*, 2017, **106**, 546–554.

14 N. Bock, A. Riminucci, C. Dionigi, A. Russo, A. Tampieri, E. Landi, V. A. Goranov, M. Marcacci and V. Dediu, A novel route in bone tissue engineering: magnetic biomimetic scaffolds, *Acta Biomater.*, 2010, **6**, 786–796.

15 *Polymeric Materials for Biomedical Implants: Characterization, Properties, and Applications*, ed. S. Thomas and A. Tharayil, Woodhead Publishing, 2024, DOI: 10.1016/C2021-0-02075-7.

16 A. Włodarczyk, S. Gorgoń, A. Radoń and K. Bajdak-Rusinek, Magnetite Nanoparticles in Magnetic Hyperthermia and Cancer Therapies: Challenges and Perspectives, *Nanomaterials*, 2022, **12**, 1807.

17 N. A. Usov and E. M. Gubanova, Application of Magnetosomes in Magnetic Hyperthermia, *Nanomaterials*, 2020, **10**(7), 1320.

18 K. D. Petrov and A. S. Chubarov, Magnetite Nanoparticles for Biomedical Applications, *Encyclopedia*, 2022, **2**, 1811–1828.

19 S. Gul, S. B. Khan, I. U. Rehman, M. Ali Khan and M. I. Khan, A Comprehensive Review of Magnetic Nanomaterials Modern Day Theranostics, *Front. Mater*, 2019, **6**, 179.

20 N. T. K. Thanh, *Magnetic Nanoparticles. From Fabrication to Clinical Applications ; Theory to Therapy, Chemistry to Clinic, Bench to Bedside*, CRC Press Taylor & Francis, Boca Raton, Fla., 2012.

21 M. O. Besenhard, A. P. LaGrow, A. Hodzic, M. Kriechbaum, L. Panariello, G. Bais, K. Loizou, S. Damilos, M. Margarida Cruz, N. T. K. Thanh and A. Gavriilidis, Co-precipitation synthesis of stable iron oxide nanoparticles with NaOH: New insights and continuous production *via* flow chemistry, *Chem. Eng. J.*, 2020, **399**, 125740.

22 C. Lindenberg, J. Schöll, L. Vicum, M. Mazzotti and J. Brozio, Experimental characterization and multi-scale modeling of mixing in static mixers, *Chem. Eng. Sci.*, 2008, **63**, 4135–4149.

23 J.-M. Lim, A. Swami, L. M. Gilson, S. Chopra, S. Choi, J. Wu, R. Langer, R. Karnik and O. C. Farokhzad, Ultra-high throughput synthesis of nanoparticles with homogeneous size distribution using a coaxial turbulent jet mixer, *ACS Nano*, 2014, **8**, 6056–6065.

24 R. Massart, Preparation of aqueous magnetic liquids in alkaline and acidic media, *IEEE Trans. Magn.*, 1981, **17**, 1247–1248.

25 S. Khalafalla and G. Reimers, Preparation of dilution-stable aqueous magnetic fluids, *IEEE Trans. Magn.*, 1980, **16**, 178–183.

26 A.-G. Niculescu, C. Chircov and A. M. Grumezescu, Magnetite nanoparticles: Synthesis methods - A comparative review, *Methods*, 2022, **199**, 16–27.

27 J. Schemberg, A. E. Abbassi, A. Lindenbauer, L.-Y. Chen, A. Grodrian, X. Nakos, G. Apte, N. Khan, A. Kraupner, T.-H. Nguyen and G. Gastrock, Synthesis of Biocompatible Superparamagnetic Iron Oxide Nanoparticles (SPION) under Different Microfluidic Regimes, *ACS Appl. Mater. Interfaces*, 2022, **14**, 48011–48028.

28 R. Abedini-Nassab, M. Pouryosef Miandoab and M. Şaşmaz, Microfluidic Synthesis, Control, and Sensing of Magnetic Nanoparticles: A Review, *Micromachines*, 2021, **12**, 768.

29 A. Baki, N. Löwa, A. Remmo, F. Wiekhorst and R. Bleul, Micromixer Synthesis Platform for a Tuneable Production of Magnetic Single-Core Iron Oxide Nanoparticles, *Nanomaterials*, 2020, **10**, 1845.

30 M. O. Besenhard, S. Pal, G. Gkogkos and A. Gavriilidis, Non-fouling flow reactors for nanomaterial synthesis, *React. Chem. Eng.*, 2023, **8**, 955–977.

31 A. H. Lu, E. L. Salabas and F. Schüth, Magnetic Nanoparticles: Synthesis, Protection, Functionalization, and Application, *Angew. Chem., Int. Ed.*, 2007, **46**, 1222–1244.

32 L. Göpfert, M. Schoenen, O. Reisen, E. M. Buhl, B. Mues, T. Schmitz-Rode and I. Slabu, Enabling continuous flow manufacturing of magnetic nanoparticles with a millifluidic system, *J. Magn. Magn. Mater.*, 2022, **563**, 169985.

33 M. O. Besenhard, L. Panariello, C. Kiefer, A. P. LaGrow, L. Storozhuk, F. Perton, S. Begin, D. Mertz, N. T. K. Thanh and A. Gavriilidis, Small iron oxide nanoparticles as MRI T1 contrast agent: scalable inexpensive water-based synthesis using a flow reactor, *Nanoscale*, 2021, **13**, 8795–8805.

34 L. Camps, L. Moens, U. Groth, L. Braeken, S. Kuhn and L. C. Thomassen, Characterization method for mass mixing in batch reactors based on temperature profiles, *Chem. Eng. Res. Des.*, 2020, **156**, 300–310.

35 C. Werner, U. König, A. Augsburg, C. Arnhold, H. Körber, R. Zimmermann and H.-J. Jacobasch, Electrokinetic surface characterization of biomedical polymers—a survey, *Colloids Surf., A*, 1999, **159**(2–3), 519–529.

36 S. Laurent, D. Forge, M. Port, A. Roch, C. Robic, L. Vander Elst and R. N. Muller, Magnetic iron oxide nanoparticles: synthesis, stabilization, vectorization, physicochemical characterizations, and biological applications, *Chem. Rev.*, 2008, **6**, 2064–2110.

37 M. Polichetti, M. Modestino, A. Galluzzi, S. Pace, M. Iuliano, P. Ciambelli and M. Sarno, Influence of citric acid and oleic acid coating on the dc magnetic properties of Fe3O4 magnetic nanoparticles, *Mater. Today: Proc.*, 2020, **20**, 21–24.

38 L. Chen, C. Yang, Y. Xiao, X. Yan, L. Hu, M. Eggersdorfer, D. Chen, D. A. Weitz and F. Ye, Millifluidics, microfluidics, and nanofluidics: manipulating fluids at varying length scales, *Mater. Today Nano*, 2021, **16**, 100136.

39 F. Yanar, A. Mosayyebi, C. Nastruzzi, D. Carugo and X. Zhang, Continuous-Flow Production of Liposomes with

© 2026 The Author(s). Published by the Royal Society of Chemistry

a Millireactor under Varying Fluidic Conditions, *Pharmaceutics*, 2020, **12**(11), 1001.
40 M. A. Levenstein, C. Chevallard, F. Malloggi, F. Testard and O. Taché, Micro- and milli-fluidic sample environments for *in situ* X-ray analysis in the chemical and materials sciences, *Lab Chip*, 2025, **25**, 1169–1227.
41 T. Sugimoto and E. Matijević, Formation of uniform spherical magnetite particles by crystallization from ferrous hydroxide gels, *J. Colloid Interface Sci.*, 1980, **74**, 227–243.
42 S. Urfels, *Synthesis and Functionalization of Magnetic Nanoparticles (Doctoral dissertation)*, Technische Universität Darmstadt, Germany, 2018, DOI: 10.26083/tuprints-00008247.
43 T. Asimakidou, A. Makridis, S. Veintemillas-Verdaguer, M. P. Morales, I. Kellartzis, M. Mitrakas, G. Vourlias, M. Angelakeris and K. Simeonidis, Continuous production of magnetic iron oxide nanocrystals by oxidative precipitation, *Chem. Eng. J.*, 2020, **393**, 124593.
44 L. Panariello, G. Wu, M. O. Besenhard, K. Loizou, L. Storozhuk, N. T. K. Thanh and A. Gavriilidis, A Modular Millifluidic Platform for the Synthesis of Iron Oxide Nanoparticles with Control over Dissolved Gas and Flow Configuration, *Materials*, 2020, **13**(4), 1019.
45 Y. Luengo, M. P. Morales, L. Gutiérrez and S. Veintemillas-Verdaguer, Counterion and solvent effects on the size of magnetite nanocrystals obtained by oxidative precipitation, *J. Mater. Chem. C*, 2016, **4**, 9482–9488.
46 R. Bleul, A. Baki, C. Freese, H. Paysen, O. Kosch and F. Wiekhorst, Continuously manufactured single-core iron oxide nanoparticles for cancer theranostics as valuable contribution in translational research, *Nanoscale Adv*, 2020, **2**, 4510–4521.
47 E. Limpert, W. A. Stahel and M. Abbt, Log-normal Distributions across the Sciences: Keys and Clues, *BioScience*, 2001, **51**, 341.
48 C. A. Schneider, W. S. Rasband and K. W. Eliceiri, NIH Image to ImageJ: 25 years of image analysis, *Nat. Methods*, 2012, **9**, 671–675.
49 H. G. Merkus, *Particle Size Measurements*, Springer Netherlands, Dordrecht, 2009.
50 W. H. Walton, Feret's Statistical Diameter as a Measure of Particle Size, *Nature*, 1948, **162**, 329–330.
51 R. R. Wildeboer, P. Southern and Q. A. Pankhurst, On the reliable measurement of specific absorption rates and intrinsic loss parameters in magnetic hyperthermia materials, *J. Phys. D: Appl. Phys.*, 2014, **47**, 495003.
52 S. R. Gadagkar and G. B. Call, Computational tools for fitting the Hill equation to dose-response curves, *J. Pharmacol. Toxicol. Methods*, 2015, **71**, 68–76.
53 F04 Committee, *Standard Practice for Marking Medical Devices and Other Items for Safety in the Magnetic Resonance Environment, ASTM F2503-20*, ASTM International, West Conshohocken, PA, 2020, DOI: 10.1520/F2503-20.
54 R. Chantrell, J. Popplewell and S. Charles, Measurements of particle size distribution parameters in ferrofluids, *IEEE Trans. Magn.*, 1978, **14**, 975–977.
55 K. O'Grady and A. Bradbury, Particle size analysis in ferrofluids, *J. Magn. Magn. Mater.*, 1983, **39**, 91–94.
56 T. Ahn, J. H. Kim, H.-M. Yang, J. W. Lee and J.-D. Kim, Formation Pathways of Magnetite Nanoparticles by Coprecipitation Method, *J. Phys. Chem. C*, 2012, **116**, 6069–6076.
57 M. Andrés Vergés, R. Costo, A. G. Roca, J. F. Marco, G. F. Goya, C. J. Serna and M. P. Morales, Uniform and water stable magnetite nanoparticles with diameters around the monodomain–multidomain limit, *J. Phys. D: Appl. Phys.*, 2008, **41**, 134003.
58 B. J. Lemaire, P. Davidson, J. Ferré, J. P. Jamet, D. Petermann, P. Panine, I. Dozov and J. P. Jolivet, Physical properties of aqueous suspensions of goethite (alpha-FeOOH) nanorods. Part I: In the isotropic phase, *EPJE*, 2004, **13**, 291–308.
59 J.-P. Jolivet, C. Chanéac and E. Tronc, Iron oxide chemistry. From molecular clusters to extended solid networks, *Chem. Commun.*, 2004, 481–487.
60 E. Asenath-Smith and L. A. Estroff, Role of Akaganeite (β-FeOOH) in the Growth of Hematite (α-Fe 2 O 3) in an Inorganic Silica Hydrogel, *Cryst. Growth Des.*, 2015, **15**, 3388–3398.
61 H. Cui, W. Ren, P. Lin and Y. Liu, Structure control synthesis of iron oxide polymorph nanoparticles through an epoxide precipitation route, *J. Exp. Nanosci.*, 2013, **8**, 869–875.
62 M. Fang, V. Ström, R. T. Olsson, L. Belova and K. V. Rao, Rapid mixing: A route to synthesize magnetite nanoparticles with high moment, *Appl. Phys. Lett.*, 2011, **99**, 222501.
63 L. Li, K. Y. Mak, C. W. Leung, K. Y. Chan, W. K. Chan, W. Zhong and P. Pong, Effect of synthesis conditions on the properties of citric-acid coated iron oxide nanoparticles, *Microelectron. Eng.*, 2013, **110**, 329–334.
64 S. M. Dadfar, D. Camozzi, M. Darguzyte, K. Roemhild, P. Varvarà, J. Metselaar, S. Banala, M. Straub, N. Güvener, U. Engelmann, I. Slabu, M. Buhl, J. van Leusen, P. Kögerler, B. Hermanns-Sachweh, V. Schulz, F. Kiessling and T. Lammers, Size-isolation of superparamagnetic iron oxide nanoparticles improves MRI, MPI and hyperthermia performance, *J. Nanobiotechnol.*, 2020, **18**, 22.
65 S. Tong, C. A. Quinto, L. Zhang, P. Mohindra and G. Bao, Size-Dependent Heating of Magnetic Iron Oxide Nanoparticles, *ACS Nano*, 2017, **11**, 6808–6816.
66 N. L. Adolphi, D. L. Huber, H. C. Bryant, T. C. Monson, D. L. Fegan, J. Lim, J. E. Trujillo, T. E. Tessier, D. M. Lovato, K. S. Butler, P. P. Provencio, H. J. Hathaway, S. A. Majetich, R. S. Larson and E. R. Flynn, Characterization of single-core magnetite nanoparticles for magnetic imaging by SQUID relaxometry, *Phys. Med. Biol.*, 2010, **55**, 5985–6003.

 © 2026 The Author(s). Published by the Royal Society of Chemistry

67 J. Rodríguez-Carvajal, Recent advances in magnetic structure determination by neutron powder diffraction, *Phys. B*, 1993, **192**, 55–69.
68 C. J. Gilmore, J. A. Kaduk and H. Schenk, Survey of computer programs for powder diffraction, *Int. Tables Crystallogr.*, 2019, **H**, 698–715.
69 I. Slabu, N. Wirch, T. Caumanns, R. Theissmann, M. Krüger, T. Schmitz-Rode and T. E. Weirich, Electron tomography and nano-diffraction enabling the investigation of individual magnetic nanoparticles inside fibers of MR visible implants, *J. Phys. D: Appl. Phys.*, 2017, **50**, 315303.
70 K. M. Krishnan, Biomedical Nanomagnetics: A Spin Through Possibilities in Imaging, Diagnostics, and Therapy, *IEEE Trans. Magn.*, 2010, **46**, 2523–2558.
71 M. Mahdavi, M. B. Ahmad, M. J. Haron, F. Namvar, B. Nadi, M. Z. A. Rahman and J. Amin, Synthesis, surface modification and characterisation of biocompatible magnetic iron oxide nanoparticles for biomedical applications, *Molecules*, 2013, **18**, 7533–7548.
72 B. Andrzejewski, W. Bednarski, M. Kaźmierczak, A. Łapiński, K. Pogorzelec-Glaser, B. Hilczer, S. Jurga, G. Nowaczyk, K. Załęski, M. Matczak, B. Łęska, R. Pankiewicz and L. Kępiński, Magnetization enhancement in magnetite nanoparticles capped with alginic acid, *Composites, Part B*, 2014, **64**, 147–154.
73 A. S. Teja and P.-Y. Koh, Synthesis, properties, and applications of magnetic iron oxide nanoparticles, *Prog. Cryst. Growth Charact. Mater.*, 2008, **55**, 22–45.
74 R. Frison, G. Cernuto, A. Cervellino, O. Zaharko, G. M. Colonna, A. Guagliardi and N. Masciocchi, Magnetite–Maghemite Nanoparticles in the 5–15 nm Range: Correlating the Core–Shell Composition and the Surface Structure to the Magnetic Properties. A Total Scattering Study, *Chem. Mater.*, 2013, **25**, 4820–4827.
75 P. Wust, U. Gneveckow, M. Johannsen, D. Böhmer, T. Henkel, F. Kahmann, J. Sehouli, R. Felix, J. Ricke and A. Jordan, Magnetic nanoparticles for interstitial thermotherapy–feasibility, tolerance and achieved temperatures, *International Journal of Hyperthermia : the Official Journal of European Society for Hyperthermic Oncology*, North American Hyperthermia Group, 2006, vol. 22, pp. 673–685.
76 I. Conde-Leboran, D. Baldomir, C. Martinez-Boubeta, O. Chubykalo-Fesenko, M. Del Puerto Morales, G. Salas, D. Cabrera, J. Camarero, F. J. Teran and D. Serantes, A Single Picture Explains Diversity of Hyperthermia Response of Magnetic Nanoparticles, *J. Phys. Chem. C*, 2015, **119**, 15698–15706.
77 R. M. Ferguson, A. P. Khandhar, C. Jonasson, J. Blomgren, C. Johansson and K. M. Krishnan, Size-Dependent Relaxation Properties of Monodisperse Magnetite Nanoparticles Measured Over Seven Decades of Frequency by AC Susceptometry, *IEEE Trans. Magn.*, 2013, **49**, 3441–3444.
78 S. Bogren, A. Fornara, F. Ludwig, M. Del Puerto Morales, U. Steinhoff, M. F. Hansen, O. Kazakova and C. Johansson, Classification of Magnetic Nanoparticle Systems–Synthesis, Standardization and Analysis Methods in the NanoMag Project, *Int. J. Mol. Sci.*, 2015, **16**, 20308–20325.
79 U. M. Engelmann, C. Shasha and I. Slabu, in *Magnetic Nanoparticles in Human Health and Medicine*, ed. C. Caizer and M. Rai, Wiley, 2021, pp. 327–354.
80 S. Dutz and R. Hergt, Magnetic nanoparticle heating and heat transfer on a microscale: Basic principles, realities and physical limitations of hyperthermia for tumour therapy, *International Journal of Hyperthermia : the Official Journal of European Society for Hyperthermic Oncology*, North American Hyperthermia Group, 2013, vol. 29, pp. 790–800.
81 M. Kallumadil, M. Tada, T. Nakagawa, M. Abe, P. Southern and Q. A. Pankhurst, Suitability of commercial colloids for magnetic hyperthermia, *J. Magn. Magn. Mater.*, 2009, **321**, 1509–1513.
82 B. Mues, B. Bauer, J. Ortega, E. M. Buhl, H. Teller, T. Gries, T. Schmitz-Rode and I. Slabu, Assessing hyperthermia performance of hybrid textile filaments: The impact of different heating agents, *J. Magn. Magn. Mater.*, 2021, **519**, 167486.
83 H. Gavilán, K. Simeonidis, E. Myrovali, E. Mazarío, O. Chubykalo-Fesenko, R. Chantrell, L. Balcells, M. Angelakeris, M. P. Morales and D. Serantes, How size, shape and assembly of magnetic nanoparticles give rise to different hyperthermia scenarios, *Nanoscale*, 2021, **13**, 15631–15646.
84 B. Mehdaoui, A. Meffre, J. Carrey, S. Lachaize, L.-M. Lacroix, M. Gougeon, B. Chaudret and M. Respaud, Optimal Size of Nanoparticles for Magnetic Hyperthermia: A Combined Theoretical and Experimental Study, *Adv. Funct. Mater.*, 2011, **21**, 4573–4581.
85 U. M. Engelmann, C. Shasha, E. Teeman, I. Slabu and K. M. Krishnan, Predicting size-dependent heating efficiency of magnetic nanoparticles from experiment and stochastic Néel-Brown Langevin simulation, *J. Magn. Magn. Mater.*, 2019, **471**, 450–456.
86 U. M. Engelmann, C. Shasha, E. Teeman, I. Slabu and K. M. Krishnan, Predicting size-dependent heating efficiency of magnetic nanoparticles from experiment and stochastic Néel-Brown Langevin simulation, *J. Magn. Magn. Mater.*, 2019, **471**, 450–456.
87 U. Engelmann, E. M. Buhl, M. Baumann, T. Schmitz-Rode and I. Slabu, Agglomeration of magnetic nanoparticles and its effects on magnetic hyperthermia, *Curr. Dir. Biomed. Eng.*, 2017, **3**, 457–460.
88 U. M. Engelmann, E. M. Buhl, S. Draack, T. Viereck, F. Ludwig, T. Schmitz-Rode and I. Slabu, Magnetic Relaxation of Agglomerated and Immobilized Iron Oxide Nanoparticles for Hyperthermia and Imaging Applications, *IEEE Magn. Lett.*, 2018, **9**, 1–5.
89 S. D. Shingte, A. H. Phakatkar, E. McKiernan, K. Nigoghossian, S. Ferguson, R. Shahbazian-Yassar and D. F. Brougham, Correlating Magnetic Hyperthermia and Magnetic Resonance Imaging Contrast Performance of

© 2026 The Author(s). Published by the Royal Society of Chemistry

Cubic Iron Oxide Nanoparticles with Crystal Structural Integrity, *Chem. Mater.*, 2022, **34**, 10801–10810.
90 M. E. de Sousa, M. B. van Fernández Raap, P. C. Rivas, P. Mendoza Zélis, P. Girardin, G. A. Pasquevich, J. L. Alessandrini, D. Muraca and F. H. Sánchez, Stability and Relaxation Mechanisms of Citric Acid Coated Magnetite Nanoparticles for Magnetic Hyperthermia, *J. Phys. Chem. C*, 2013, **117**, 5436–5445.
91 R. Hergt and S. Dutz, Magnetic particle hyperthermia—biophysical limitations of a visionary tumour therapy, *J. Magn. Magn. Mater.*, 2007, **311**, 187–192.
92 A. Bhardwaj, K. Parekh and N. Jain, In vitro hyperthermic effect of magnetic fluid on cervical and breast cancer cells, *Sci. Rep.*, 2020, **10**, 15249.
93 L. Storozhuk, M. O. Besenhard, S. Mourdikoudis, A. P. LaGrow, M. R. Lees, D. Le Tung, A. Gavriilidis and N. T. K. Thanh, Stable Iron Oxide Nanoflowers with Exceptional Magnetic Heating Efficiency: Simple and Fast Polyol Synthesis, *ACS Appl. Mater. Interfaces*, 2021, **13**, 45870–45880.
94 H. Etemadi and P. G. Plieger, Magnetic Fluid Hyperthermia Based on Magnetic Nanoparticles: Physical Characteristics, Historical Perspective, Clinical Trials, Technological Challenges, and Recent Advances, *Adv. Ther.*, 2020, **3**(11), 2000061.
95 Y. Hadadian, A. P. Ramos and T. Z. Pavan, Role of zinc substitution in magnetic hyperthermia properties of magnetite nanoparticles: interplay between intrinsic properties and dipolar interactions, *Sci. Rep.*, 2019, **9**, 18048.
96 R. Qiao, C. Yang and M. Gao, Superparamagnetic iron oxide nanoparticles: from preparations to *in vivo* MRI applications, *J. Mater. Chem.*, 2009, **19**, 6274.
97 Y.-W. Jun, Y.-M. Huh, J.-S. Choi, J.-H. Lee, H.-T. Song, S. Kim, S. Yoon, K.-S. Kim, J.-S. Shin, J.-S. Suh and J. Cheon, Nanoscale size effect of magnetic nanocrystals and their utilization for cancer diagnosis *via* magnetic resonance imaging, *J. Am. Chem. Soc.*, 2005, **127**, 5732–5733.
98 M. A. Oghabian and N. M. Farahbakhsh, Potential use of nanoparticle based contrast agents in MRI: a molecular imaging perspective, *J. Biomed. Nanotechnol.*, 2010, **6**, 203–213.
99 Z. Hai, Y. Ni, D. Saimi, H. Yang, H. Tong, K. Zhong and G. Liang, γ-Glutamyltranspeptidase-Triggered Intracellular Gadolinium Nanoparticle Formation Enhances the T2-Weighted MR Contrast of Tumor, *Nano Lett.*, 2019, **19**, 2428–2433.
100 D. Y. Lee, Highly effective T2 MR contrast agent based on heparinized superparamagnetic iron oxide nanoparticles, *Macromol. Res.*, 2011, **19**, 843–847.
101 X. Huang, Y. Yuan, W. Ruan, L. Liu, M. Liu, S. Chen and X. Zhou, pH-responsive theranostic nanocomposites as synergistically enhancing positive and negative magnetic resonance imaging contrast agents, *J. Nanobiotechnol.*, 2018, **16**, 30.
102 Z. Zhao, M. Li, J. Zeng, L. Huo, K. Liu, R. Wei, K. Ni and J. Gao, Recent advances in engineering iron oxide nanoparticles for effective magnetic resonance imaging, *Bioact. Mater.*, 2022, **12**, 214–245.
103 J. Mohapatra, A. Mitra, H. Tyagi, D. Bahadur and M. Aslam, Iron oxide nanorods as high-performance magnetic resonance imaging contrast agents, *Nanoscale*, 2015, **7**, 9174–9184.
104 T. Yoshida, T. Nakamura, O. Higashi and K. Enpuku, Magnetic fractionation and characterization of magnetic nanoparticles for magnetic particle imaging, *Jpn. J. Appl. Phys.*, 2018, **57**, 80302.
105 L. Moor, S. Scheibler, L. Gerken, K. Scheffler, F. Thieben, T. Knopp, I. K. Herrmann and F. H. L. Starsich, Particle interactions and their effect on magnetic particle spectroscopy and imaging, *Nanoscale*, 2022, **14**, 7163–7173.
106 S. Behzadi, V. Serpooshan, W. Tao, M. A. Hamaly, M. Y. Alkawareek, E. C. Dreaden, D. Brown, A. M. Alkilany, O. C. Farokhzad and M. Mahmoudi, Cellular uptake of nanoparticles: journey inside the cell, *Chem. Soc. Rev.*, 2017, **46**, 4218–4244.
107 S. E. A. Gratton, P. A. Ropp, P. D. Pohlhaus, J. C. Luft, V. J. Madden, M. E. Napier and J. M. DeSimone, The effect of particle design on cellular internalization pathways, *Proc. Natl. Acad. Sci. U. S. A.*, 2008, **105**, 11613–11618.
108 M. Balk, T. Haus, J. Band, H. Unterweger, E. Schreiber, R. P. Friedrich, C. Alexiou and A.-O. Gostian, Cellular SPION Uptake and Toxicity in Various Head and Neck Cancer Cell Lines, *Nanomaterials*, 2021, **11**, 726.
109 A. Plan Sangnier, A. B. van de Walle, A. Curcio, R. Le Borgne, L. Motte, Y. Lalatonne and C. Wilhelm, Impact of magnetic nanoparticle surface coating on their long-term intracellular biodegradation in stem cells, *Nanoscale*, 2019, **11**, 16488–16498.
110 I. Slabu, A. A. Roeth, U. M. Engelmann, F. Wiekhorst, E. M. Buhl, U. P. Neumann and T. Schmitz-Rode, Modeling of magnetoliposome uptake in human pancreatic tumor cells in vitro, *Nanotechnology*, 2019, **30**, 184004.
111 C. Wilhelm, C. Billoteya, J. Rogerc, J. N. Pons, J.-C. Bacri and F. Gazeau, Intracellular uptake of anionic superparamagnetic nanoparticles as a function of their surface coating, *Biomaterials*, 2002, **24**, 1001–1011.
112 J. Liu, C. Dai and Y. Hu, Aqueous aggregation behavior of citric acid coated magnetite nanoparticles: Effects of pH, cations, anions, and humic acid, *Environ. Res.*, 2018, **161**, 49–60.
113 X. Wu, Y. Tan, H. Mao and M. Zhang, Toxic effects of iron oxide nanoparticles on human umbilical vein endothelial cells, *Int. J. Nanomed.*, 2010, **5**, 385–399.
114 M. Pooresmaeil, S. Javanbakht, H. Namazi and A. Shaabani, Application or function of citric acid in drug delivery platforms, *Med. Res. Rev.*, 2021, **42**, 800–849.
115 M. Wagner, S. Wagner, J. Schnorr, E. Schellenberger, D. Kivelitz, L. Krug, M. Dewey, M. Laule, B. Hamm and M. Taupitz, Coronary MR angiography using citrate-coated very small superparamagnetic iron oxide particles

 © 2026 The Author(s). Published by the Royal Society of Chemistry

as blood-pool contrast agent: Initial experience in humans, *J. Magn. Reson. Imaging*, 2011, **34**, 816–823.
116 C. Corot, P. Robert, J.-M. Idée and M. Port, Recent advances in iron oxide nanocrystal technology for medical imaging, *Adv. Drug Delivery Rev.*, 2006, **58**, 1471–1504.
117 J. Li, H. Mao, N. Kawazoe and G. Chen, Insight into the interactions between nanoparticles and cells, *Biomater. Sci.*, 2017, **5**, 173–189.
118 S. E. Sandler, B. Fellows and O. T. Mefford, Best Practices for Characterization of Magnetic Nanoparticles for Biomedical Applications, *Anal. Chem.*, 2019, **91**, 14159–14169.
119 K. El-Boubbou, Magnetic iron oxide nanoparticles as drug carriers: clinical relevance, *Nanomedicine*, 2018, **13**, 953–971.
120 N. J. Serkova, Nanoparticle-Based Magnetic Resonance Imaging on Tumor-Associated Macrophages and Inflammation, *Front. Immunol.*, 2017, **8**, 590.
121 J. S. Weinstein, C. G. Varallyay, E. Dosa, S. Gahramanov, B. Hamilton, W. D Rooney, L. L. Muldoon and E. A. Neuwelt, Superparamagnetic Iron Oxide Nanoparticles: Diagnostic Magnetic Resonance Imaging and Potential Therapeutic Applications in Neurooncology and Central Nervous System Inflammatory Pathologies, a Review, *J. Cereb. Blood Flow Metab.*, 2010, **1**, 15–35.
122 L. Pasquini, A. Napolitano, E. Visconti, D. Longo, A. Romano, P. Tomà and M. C. Rossi Espagnet, Gadolinium-Based Contrast Agent-Related Toxicities, *CNS Drugs*, 2018, **32**, 229–240.
123 E. Lancelot, Revisiting the Pharmacokinetic Profiles of Gadolinium-Based Contrast Agents: Differences in Long-Term Biodistribution and Excretion, *Invest. Radiol.*, 2016, **51**, 691–700.
124 M. Ramalho, J. Ramalho, L. M. Burke and R. C. Semelka, Gadolinium Retention and Toxicity-An Update, *ACKD*, 2017, **24**, 138–146.
125 A. J. Grippin, B. Wummer, T. Wildes, K. Dyson, V. Trivedi, C. Yang, M. Sebastian, H. R. Mendez-Gomez, S. Padala, M. Grubb, M. Fillingim, A. Monsalve, E. J. Sayour, J. Dobson and D. A. Mitchell, Dendritic Cell-Activating Magnetic Nanoparticles Enable Early Prediction of Antitumor Response with Magnetic Resonance Imaging, *ACS Nano*, 2019, **13**, 13884–13898.
126 T. Hardwick and N. Ahmed, Digitising chemical synthesis in automated and robotic flow, *Chem. Sci.*, 2020, **11**, 11973–11988.
127 H. Tao, T. Wu, S. Kheiri, M. Aldeghi, A. Aspuru-Guzik and E. Kumacheva, Self-Driving Platform for Metal Nanoparticle Synthesis: Combining Microfluidics and Machine Learning, *Adv. Funct. Mater.*, 2021, **31**(51), 2106725.
128 A. A. Volk, R. W. Epps, D. T. Yonemoto, B. S. Masters, F. N. Castellano, K. G. Reyes and M. Abolhasani, AlphaFlow: autonomous discovery and optimization of multi-step chemistry using a self-driven fluidic lab guided by reinforcement learning, *Nat. Commun.*, 2023, **14**, 1403.
129 N. Mukhin, P. Jha and M. Abolhasani, The role of flow chemistry in self-driving labs, *Matter*, 2025, **8**, 102205.
130 N. Löwa, D. Gutkelch, E.-A. Welge, R. Welz, F. Meier, A. Baki, R. Bleul, T. Klein and F. Wiekhorst, Novel Benchtop Magnetic Particle Spectrometer for Process Monitoring of Magnetic Nanoparticle Synthesis, *Nanomaterials*, 2020, **10**(11), 2277.
131 M. S. Baig, M. A. Haque, T. K. R. Konatham, B. D. Mohammad, B. A. Yahya, S. S. Saffiruddin, F. A. Siddiqui and S. L. Khan, Recent advancements in hyperthermia-driven controlled drug delivery from nanotherapeutics, *Recent Adv. Drug Deliv. Formul.*, 2022, **16**(4), 270–286.
132 H. Wang, S. Zhao, J. Zhou, K. Zhu, X. Cui, W. Huang, M. N. Rahaman, C. Zhang and D. Wang, Biocompatibility and osteogenic capacity of borosilicate bioactive glass scaffolds loaded with Fe3O4 magnetic nanoparticles, *J. Mater. Chem. B*, 2015, **3**, 4377–4387.
133 M. Li, J. Liu, X. Cui, G. Sun, J. Hu, S. Xu, F. Yang, L. Zhang, X. Wang and P. Tang, Osteogenesis effects of magnetic nanoparticles modified-porous scaffolds for the reconstruction of bone defect after bone tumor resection, *Regener. Biomater.*, 2019, **6**, 373–381.
134 G. Köhler, H. Wundsam, L. Pallwein-Prettner, O. O. Koch and K. Emmanuel, Magnetic resonance visible 3-D funnel meshes for laparoscopic parastomal hernia prevention and treatment, *Eur. Surg. Res.*, 2015, **47**, 127–132.
135 D. Hensley, Z. W. Tay, R. Dhavalikar, P. Goodwill, B. Zheng, C. Rinaldi and S. Conolly, in *Energy-based Treatment of Tissue and Assessment IX*, ed. T. P. Ryan, SPIE, 2017, p. 1006603.
136 Y. Lu, A. Rivera-Rodriguez, Z. W. Tay, D. Hensley, K. L. B. Fung, C. Colson, C. Saayujya, Q. Huynh, L. Kabuli, B. Fellows, P. Chandrasekharan, C. Rinaldi and S. Conolly, Combining magnetic particle imaging and magnetic fluid hyperthermia for localized and image-guided treatment, *International Journal of Hyperthermia : the Official Journal of European Society for Hyperthermic Oncology*, North American Hyperthermia Group, 2020,vol. 37, pp. 141–154.
137 P. Ludewig, N. Gdaniec, J. Sedlacik, N. D. Forkert, P. Szwargulski, M. Graeser, G. Adam, M. G. Kaul, K. M. Krishnan, R. M. Ferguson, A. P. Khandhar, P. Walczak, J. Fiehler, G. Thomalla, C. Gerloff, T. Knopp and T. Magnus, Magnetic Particle Imaging for Real-Time Perfusion Imaging in Acute Stroke, *ACS Nano*, 2017, **11**, 10480–10488.
138 E. U. Saritas, P. W. Goodwill, L. R. Croft, J. J. Konkle, K. Lu, B. Zheng and S. M. Conolly, Magnetic particle imaging (MPI) for NMR and MRI researchers, *J. Magn. Reson.*, 2013, **229**, 116–126.
139 O. L. Lanier, O. I. Korotych, A. G. Monsalve, D. Wable, S. Savliwala, N. W. F. Grooms, C. Nacea, O. R. Tuitt and J. Dobson, Evaluation of magnetic nanoparticles for magnetic fluid hyperthermia, *Int. J. Hyperthermia*, 2019, **36**, 686–700.

© 2026 The Author(s). Published by the Royal Society of Chemistry